bioRxiv preprint doi: https://doi.org/10.1101/2022.05.23.492966; this version posted May 24, 2022. The copyright holder for this preprint (which was not certified by peer review) is the author/funder, who has granted bioRxiv a license to display the preprint in perpetuity. It is made available under aCC-BY-NC 4.0 International license.

Cellular segregation in co-cultures driven by differential adhesion and contractility on distinct time scales

Mark Skamrahl, Justus Schünemann, Markus Mukenhirn, Jannis Gottwald, Maximilian Ferle, Angela Rübeling, Alf Honigmann, Andreas Janshoff*

M. Skamrahl, J. Schünemann, J. Gottwald, M. Ferle, Prof. Dr. A. Janshoff
University of Göttingen, Institute of Physical Chemistry,
Tammannstr. 6, 37077 Göttingen, Germany
*E-mail: ajansho@gwdg.de

A. Rübeling
University of Göttingen, Institute of Organic and Biomolecular Chemistry,
Tammannstr. 2, 37077 Göttingen, Germany

Dr. M. Mukenhirn, Prof. Dr. A. Honigmann
Max Planck Institute of Molecular Cell Biology and Genetics,
Pfotenhauerstraße 108, 01307 Dresden, Germany

Keywords: cell sorting, differential interfacial tension hypothesis, contractility, adhesion, tight junctions

Abstract

Cellular sorting and pattern formation is crucial for many biological processes such as development, tissue regeneration, and cancer progression. Prominent physical driving forces for cellular sorting are differential adhesion and contractility. Here, we studied the segregation of epithelial co-cultures containing highly contractile, ZO1/2-depleted MDCKII cells (dKD) and their wildtype (WT) counterparts using multiple quantitative, high-throughput methods to monitor their dynamical and mechanical properties. We observe a time-dependent segregation process, governed mainly by differential contractility on short (< 5 h) and differential adhesion on long (> 5 h) time scales, respectively. The overly contractile dKD cells exert strong lateral forces on their WT neighbors, thereby apically depleting their surface area. This is reflected in a six-fold difference in excess surface area between both cell types. The lateral forces lead to a four- to six-fold increase in tension at all junctions that are in contact with the contractile cells including the interface between heterotypic cell-cell contacts. Concomitantly, the tight junction-depleted, contractile cells exhibit weaker cell-cell adhesion. Drug-induced contractility reduction delays the initial segregation but ceases to change the final demixed state, rendering differential adhesion the dominant segregation force at longer time scales.

bioRxiv preprint doi: https://doi.org/10.1101/2022.05.23.492966; this version posted May 24, 2022. The copyright holder for this preprint (which was not certified by peer review) is the author/funder, who has granted bioRxiv a license to display the preprint in perpetuity. It is made available under aCC-BY-NC 4.0 International license.

This well-controlled model system shows how cell sorting is accomplished through a complex interplay between differential adhesion and contractility and can be explained largely by generic physical driving forces.

Introduction

Cellular sorting and tissue separation are essential processes in embryogenesis and tissue development, studied across multiple species.[1,2] Early work has shown that cells taken from different embryonic tissues and remixed together eventually segregate, or demix, again.[3,4] Sorting of cells in tissues can be governed by different biological and physical factors. Owing to our accumulated knowledge about cell-cell junctions and the cytoskeleton, a hypothesis for cellular demixing based on differential adhesion was proposed.[5,6] To accommodate different biological scenarios, this first hypothesis was complemented by incorporating differential cell contractility.[7,8] Adhesion- and contractility-induced tensions basically act antagonistically: Contractility induces cell rounding to minimize the contact zone, whereas adhesion enlarges the cell-cell contact region. The resulting surface tension of the tissue is the ratio of adhesion and contractility.[9] This view has been extended more recently by the addition of local contractile cues, for example in the anteroposterior compartment boundary in Drosophila flies.[10–12] Alternatively, active cell forces have been proposed to also play a role in regulating cellular demixing in co-cultures.[13] However, it remains difficult to differentiate between the various factors that govern cell sorting. In recent years, many simulation-based studies characterized different physical driving forces of demixing, identifying many possible pathways to cellular segregation via differential physical cell properties.[9,14–22] Such simulations have the idea in common that the overall free energy in a cell layer, as determined by parameters such as contractility and adhesion, needs to be minimized. However, fundamental experimental evidence remains scarce, only applicable in certain scenarios, and often correlative.

Recently, it has been shown that in tight junction-depleted epithelial cells (ZO1 and 2 knockdown; abbreviated as dKD) two distinct cell populations emerge: some cells contract and by that adopt a roundish shape; pulling on their neighbors eventually results in laterally elongated cells that coexist with the contracted cells.[23,24] In initial experiments, the stretched cell population was successfully replaced by less contractile wildtype (WT) cells, substantially increasing the mismatch in mechanical properties. In this co-culture, overly contractile dKD cells inhibited layer fluidity and migration by means of jamming. However, the driving forces for segregation in such a co-culture remain to be elucidated.

bioRxiv preprint doi: https://doi.org/10.1101/2022.05.23.492966; this version posted May 24, 2022. The copyright holder for this preprint (which was not certified by peer review) is the author/funder, who has granted bioRxiv a license to display the preprint in perpetuity. It is made available under aCC-BY-NC 4.0 International license.

Here, we now address this question by studying co-cultures of dKD and WT cells using high-throughput/content (de-) mixing experiments in combination with quantitative mechanical measurements. We focus on the quantification of cellular viscoelasticity, contractility, and cell-cell as well as cell-substrate adhesion to shine light on the emergence and persistence of segregated cell monolayers. We found that a time-dependent demixing process in these co-cultured monolayers is governed by differential contractility on short time scales (within the first five hours), while on longer time scales (> 5 h) differential adhesion prevails. Such separation of demixing time scales has not been observed before. In addition, we show that the overly contractile dKD cells stretch out their WT neighbors and apically depleting their excess surface area, with a six-fold difference between the cell types. The dKD contractility leads to an about four- to six-fold increase in tension at all junctions in contact with these cells including the interface between heterotypic cell contacts. Additionally, the tight junction-compromised, contractile dKD cells exhibit weaker cell-cell adhesion. Taken together, our experimental results indicate that differential interfacial tension prevails in the beginning to segregate the cell types, while with elapsed time differential adhesion becomes more and more important for demixing.

Results

Demixing of highly contractile dKD and compliant WT cell co-cultures

First, live cell (de-) mixing experiments were recorded directly after thorough mixing and seeding using phase contrast and fluorescence microscopy (Figure 1A). We used WT cells with a GFP tag, (named WT-GFP from here on, see methods section) to distinguish them from dKD cells. Cell segmentation and neighbor analysis using both the fluorescence signal and phase contrast images allowed for automatic assignment of cells as WT or dKD. This enabled us to quantify how much the cells mixed randomly or demixed into clusters, also called segregation. Therefore, we defined a segregation index *SI* as the number of homotypic neighbors divided by the number of all neighbors.

In the case of a completely random cell distribution, an average segregation index of 0.5 would be expected. However, this parameter is also impacted by natural, local processes such as cell division. To account for these deviations from randomness, we performed control experiments using a pseudo co-culture consisting of WT-GFP cells and unmodified WT cells.

bioRxiv preprint doi: https://doi.org/10.1101/2022.05.23.492966; this version posted May 24, 2022. The copyright holder for this preprint (which was not certified by peer review) is the author/funder, who has granted bioRxiv a license to display the preprint in perpetuity. It is made available under aCC-BY-NC 4.0 International license.

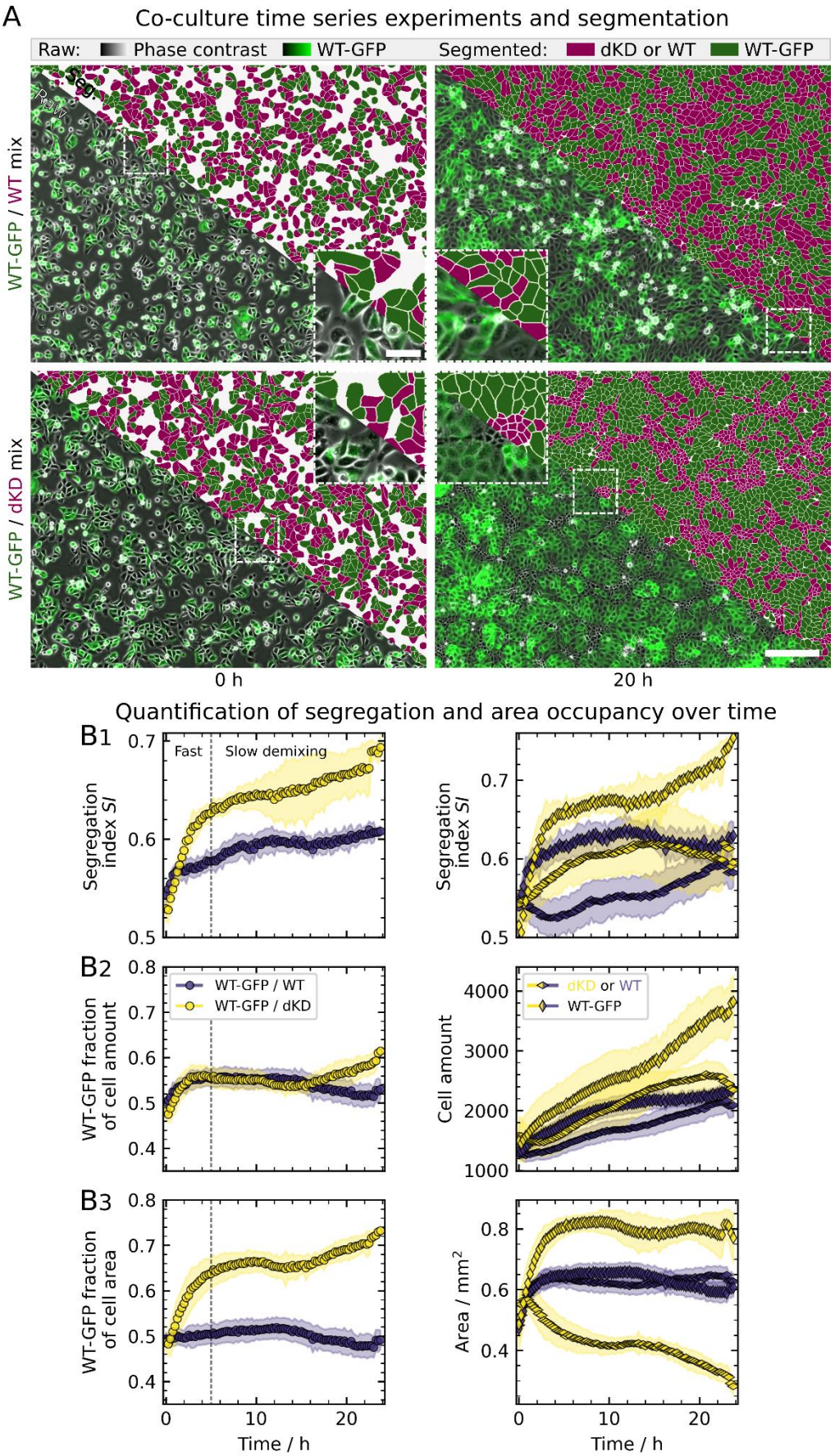

bioRxiv preprint doi: https://doi.org/10.1101/2022.05.23.492966; this version posted May 24, 2022. The copyright holder for this preprint (which was not certified by peer review) is the author/funder, who has granted bioRxiv a license to display the preprint in perpetuity. It is made available under aCC-BY-NC 4.0 International license.

Figure 1. Demixing behavior of dKD and WT cell co-cultures at an initial mixing ratio of 50:50. A) Example overlay of phase contrast (grayscale) and fluorescence (green: WT-GFP cells) channels with corresponding segmentations (green: WT-GFP, magenta: dKD cells in WT-GFP/dKD mix or WT in WT-GFP/WT control, respectively). Samples were imaged immediately after seeding and mounting on the microscope (0 h). Scale bars: 200 µm and 50 µm (zoom-in). B) Demixing, cell amount, and area occupancy quantification. The vertical dashed line at 5 h indicates two distinct demixing time scales. B1) The segregation index *SI*, defined as the average ratio of homotypic and all cell neighbors, quantifies the demixing degree. The *SI* is shown averaged over both cell types (left) as well as separately for each cell type (right). B2) Left: Relative cell amount, calculated as the ratio of the amount of WT-GFP cells and the total cell amount. Right: Total cell amounts of each cell type. B3) Left: WT-GFP fraction of the overall cell area, calculated as the ratio of the WT-GFP area and the total cell area, indicating contractility discrepancies between the cell types. Right: Total covered area of each cell type. Corresponding distributions of the individual cell areas are depicted in Figure S1. Means and standard deviations are shown. 12 separate regions from 6 culture dishes, acquired on three separate days (two regions per dish, two dishes per day), were measured and are shown per co-culture mix.

After detaching the cells and mixing the suspensions thoroughly prior to seeding, initially, both the WT/WT control as well as the WT/dKD mixture showed a segregation index close to 0.5 (Figure 1B1). The slight shift to higher values was likely already introduced upon initial seeding when most cells were still sedimenting, while others were already attached. Within the first hour, both co-cultures initially demixed from about 0.52 to 0.57 (Figure 1B1). However, after this time only the WT/dKD mixture segregated further, as expected. The *SI* increased to about 0.63 within the first 5 h, whereas the control remained at 0.57. After this fast initial demixing, both co-cultures segregated further at a similar rate to reach values close to 0.7 for the WT/dKD and 0.6 for the WT/WT cells.

In co-culture with dKD, WT cells sorted into large, preferentially round clusters (Figure 1A) with a higher average *SI* than their dKD counterparts (Figure 1B1, on the right). The dKD cells, with a lower *SI*, were arranged in elongated, string-like clusters around the WT domains. In contrast, the WT/WT control showed an inconspicuous and less defined layer morphology. The *SI* of the labeled WT cells was generally higher than that of the unlabeled ones. However, this *SI*-difference vanished over time in the WT/WT co-culture, whereas in the WT/dKD mixture it even increased. Accordingly, WT/dKD co-cultures exhibited a sorting behavior into distinct clusters, different from homotypic monolayers.

bioRxiv preprint doi: https://doi.org/10.1101/2022.05.23.492966; this version posted May 24, 2022. The copyright holder for this preprint (which was not certified by peer review) is the author/funder, who has granted bioRxiv a license to display the preprint in perpetuity. It is made available under aCC-BY-NC 4.0 International license.

As a control/normalization parameter for the *SI*, we next examined the cell amount of both cell types in each co-culture, because a difference in the relative cell amount could influence the *SI* as well. However, we observed no difference in the relative cell amount (WT-GFP fraction of the cell amount in Figure 1B2) between the WT/WT control and the WT/dKD cells. Interestingly, the total cell amount differed, with overall higher proliferation rates and larger cell amounts in the WT/dKD mixture. After a short delay in dKD cell proliferation, the dKD increased at a similar rate as the WT-GFP amount until about 15 h after seeding. Importantly, the resulting small difference in the cell amount between the cell types was present in both the WT/dKD co-culture and WT/WT control, slightly biasing the *SI* of both to larger values. After 15 h, dKD cells started to extrude apically out of the layer, offsetting proliferation and thereby stalling the cell amount. In the WT/WT mixture, the WT-GFP also showed slightly more proliferation until 15 h after seeding, which then leveled off.

Next, to examine the cell contractility discrepancy of these cell lines, which was described previously[23,24], we first quantified the labeled WT fraction of the cell area (Figure 1B3). If there were no discrepancies in contractility in the co-culture, this parameter would be expected to be 0.5 because each cell type would occupy 50% of the covered area. Indeed, this was the case for the WT/WT control. In contrast, however, the WT/dKD co-cultures showed a strong increase of the WT area fraction within the first 5 h, nicely correlating with the *SI* increase. This highlights a great differential contractility with highly contractile dKD cells occupying smaller areas and stretched WT cells covering more space on the culture dish. At the same time, as described before, the cell number ratio stayed constant, confirming that the larger area coverage of WT cells is due to lateral extension provoked by contractile dKD cells and not a consequence of an increased amount of WT cells. Notably, this effect only develops over time due to collective cell-cell interactions because the WT/dKD mixture also starts out at *SI* = 0.5. However, the contractile discrepancy is generally underestimated here. This is because the phase contrast channel was used for analysis (the fluorescence was only used to assign the cell type, see methods section) but the lateral stretching of bordering WT cells by dKD neighbors can be best observed in the WT-GFP specific fluorescence channel (white arrows in Figure 2B). This is because the WT cell body extension, even overlapping above dKD cells, is specifically seen in the GFP channel (Figure 2B) while in phase contrast, the overlapping WT and dKD cell bodies cannot be distinguished well (Figure 1A).

bioRxiv preprint doi: https://doi.org/10.1101/2022.05.23.492966; this version posted May 24, 2022. The copyright holder for this preprint (which was not certified by peer review) is the author/funder, who has granted bioRxiv a license to display the preprint in perpetuity. It is made available under aCC-BY-NC 4.0 International license.

Differential actomyosin contractility and 3D cell morphology of WT/dKD co-cultures

To further study the differential contractility of WT/dKD co-cultures on a molecular and cell morphological level, we applied confocal fluorescence microscopy and AFM imaging (Figure 2).

In accordance with previous work[23], we observed a strong actomyosin upregulation at the apical-lateral cell periphery of dKD cells (Figure 2A). Particularly, activated (phosphorylated) myosin accumulated at the apical cell-cell junctions. A thick perijunctional actomyosin ring was formed, constricting the cells apically. Conversely, the WT cells did not show any upregulation of phosphorylated myosin or of the actin cytoskeleton. To conserve the cellular volume, dKD cells were forced to bulge out apically. Since all dKD cells were still connected to their neighbors, adjacent WT cells were stretched out and flattened by the apical pull of the dKD cells. Strikingly, WT cells at the WT/dKD interface were partially pulled across their direct dKD neighbors towards the center of the dKD cluster (Figure 2B, white arrows). Note that this lateral pulling translocates certain cell components, such as ZO1 or myosin in Figure 2A and B, relative to the nucleus. The lateral elongation of WT and apical contraction of dKD cells was confirmed by AFM imaging (Figure 2C). Interestingly, the bordering junctions at the interface between a WT and dKD cluster are particularly pronounced on the apical side (Figure 2C). This was mirrored by an increased myosin accumulation in this region (Figure 2B), which, taken together, highlights the mechanical discrepancy between the cell types.

bioRxiv preprint doi: https://doi.org/10.1101/2022.05.23.492966; this version posted May 24, 2022. The copyright holder for this preprint (which was not certified by peer review) is the author/funder, who has granted bioRxiv a license to display the preprint in perpetuity. It is made available under aCC-BY-NC 4.0 International license.

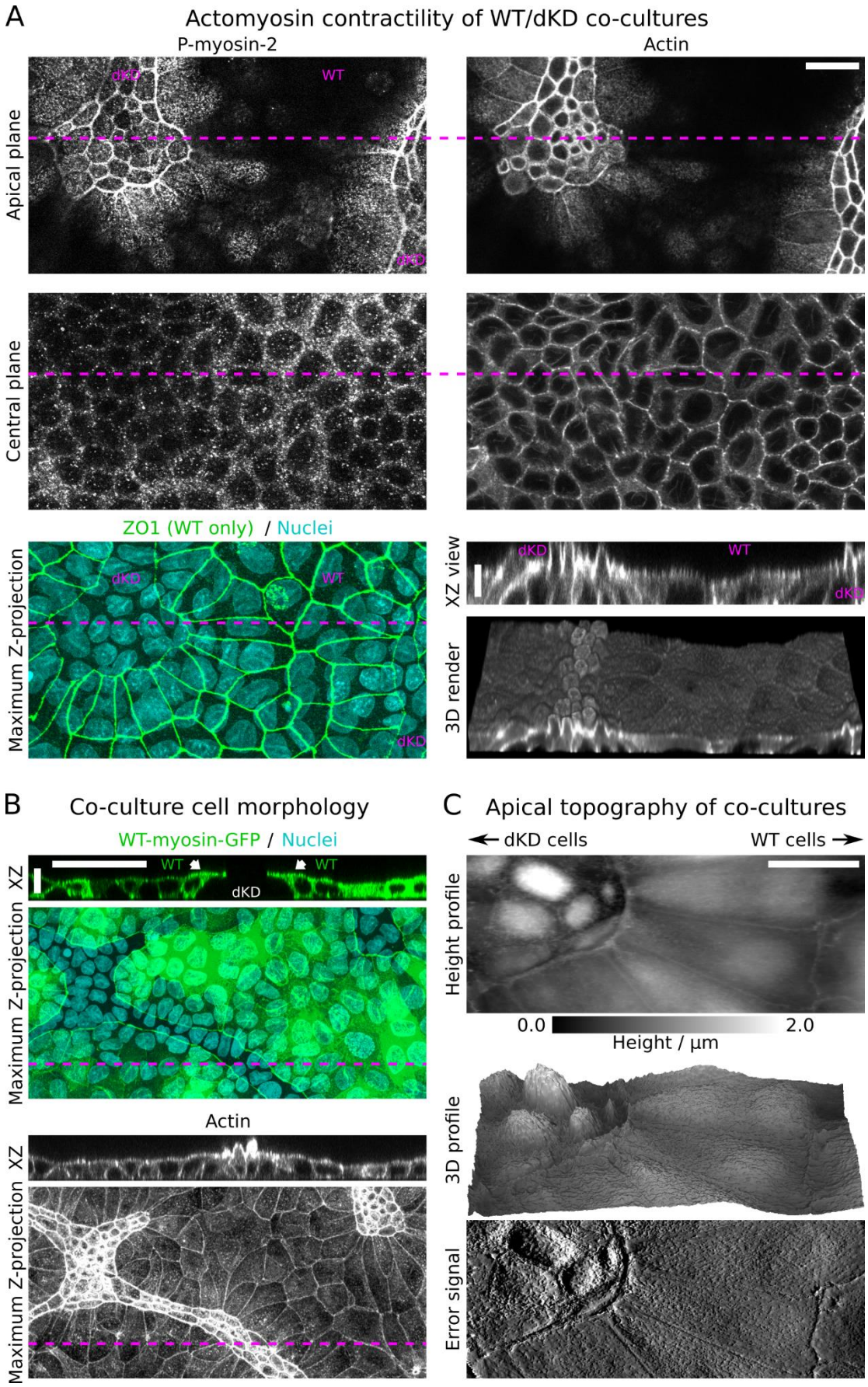

bioRxiv preprint doi: https://doi.org/10.1101/2022.05.23.492966; this version posted May 24, 2022. The copyright holder for this preprint (which was not certified by peer review) is the author/funder, who has granted bioRxiv a license to display the preprint in perpetuity. It is made available under aCC-BY-NC 4.0 International license.

Figure 2. Differential actomyosin contractility of WT/dKD co-cultures. A) Representative WT/dKD co-cultures co-stained for phosphorylated myosin (P-myosin-2 antibody), actin (phalloidin), nuclei (DAPI, cyan), and ZO1 (ZO1 antibody, green). ZO1 was used to distinguish ZO1/2 dKD from WT cells. Magenta lines indicate location of the XZ view. XY scale bar: 20 µm, Z: 5 µm. B) WT-GFP/dKD co-culture co-stained for actin (phalloidin) and nuclei (DAPI, cyan). The green channel was used to identify the WT-GFP cells and to examine their morphology in 3D. XY scale bar: 50 µm, Z: 10 µm. C) Apical topography of WT-GFP/dKD co-cultures obtained by AFM imaging. Height profile, the corresponding 3D topography map which was up-scaled vertically by 50%, and error signal (deflection image). Scale bar: 20 µm. Cells in A were fixed after 28 h, and in B and C after about 48 h of growth.

Differential mechanics of dKD and WT cells in co-culture

To directly quantify the mechanical consequences of the described contractile, molecular, and morphological disparities in WT/dKD co-cultures, we examined their mechanical phenotypes by AFM indentation-relaxation as well as laser ablation (Figure 3).

First, we acquired AFM indentation maps (Figure 3A) and examined the apparent local stiffness, which is reflected in the slope of the force-distance curve. Here, we observed a similar picture as in pure dKD monolayers,[23] dKD cells were softer at the central cortex and extremely stiff at the perijunctional actomyosin ring (vide supra). In contrast, neighboring WT cells showed only slightly pronounced cell boundaries but an increased stiffness at the center in comparison with dKD neighbors.

To further characterize this stiffness difference at the center of the two cell types, we performed site-specific indentation experiments followed by force relaxation and applied a tailor-made viscoelastic fitting model as described in several recent studies.[23,25,26] In brief, this model fits the stress relaxation of the composite viscoelastic shell upon indentation according to a power law of the area compressibility modulus. Importantly, the cell geometry (area and angle of the apical cap), which differs tremendously between both cell lines (vide supra), can be adjusted in this model (Figure 3B). Three parameters are obtained: the prestress T_0 corresponding to the actomyosin cortex tension, the apparent area compressibility modulus K_A, which mirrors the excess cell surface area, and the fluidity β representing the viscous behavior (energy dissipation) of the cortex. A β value of 1 corresponds to a Newtonian fluid, whereas $\beta = 0$ refers to an elastic solid.

bioRxiv preprint doi: https://doi.org/10.1101/2022.05.23.492966; this version posted May 24, 2022. The copyright holder for this preprint (which was not certified by peer review) is the author/funder, who has granted bioRxiv a license to display the preprint in perpetuity. It is made available under aCC-BY-NC 4.0 International license.

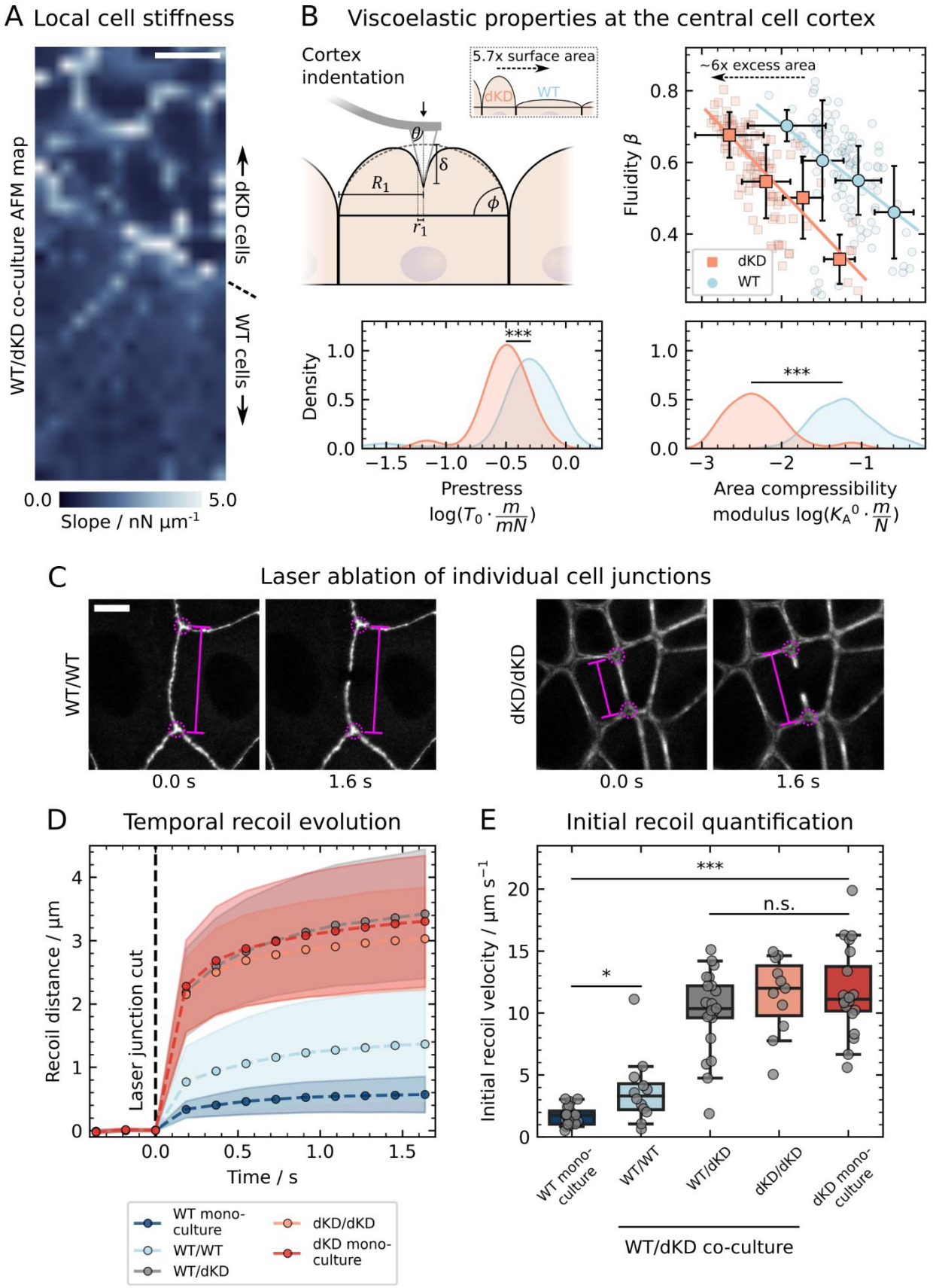

bioRxiv preprint doi: https://doi.org/10.1101/2022.05.23.492966; this version posted May 24, 2022. The copyright holder for this preprint (which was not certified by peer review) is the author/funder, who has granted bioRxiv a license to display the preprint in perpetuity. It is made available under aCC-BY-NC 4.0 International license.

Figure 3. Differential mechanical properties of dKD and WT cells in co-culture. A) AFM map showing the slope of the force curve during contact, which locally reflects the apparent mechanical stiffness. Scale bar: 10 µm. B) Site-specific viscoelastic properties of the central cell cortex in proximity to the WT/dKD interface. The cortex indentation geometry considered in the Evans model includes the contact angle ϕ and base radius R_1 of the spherical cell cap, the indentation depth δ and the contact radius r_1. Importantly, dKD cells had a pronounced cap with larger ϕ and smaller R_1 than WT cells (vide supra), yielding a 5.7-fold surface area difference. Upon fitting, the fluidity β was plotted against the decade logarithm of the area compressibility modulus K_A^0, and histograms for the latter and the prestress T_0 are shown. Small transparent data points represent individual indentations. Large symbols and error bars are binned means and standard deviations. Lines indicate linear fits (in log space) of the binned means. C) Laser ablation examples of individual cell junctions. In WT cells, ZO1 in the tight junctions was stained, and in dKD cells, myosin was stained. D) Tensile junction properties were obtained by tracking the distance (magenta lines) between two opposing junction vertices (magenta circles) upon recoil. Temporal means and standard deviations are shown. E) The initial recoil velocity was calculated between the last point before (0.00 s) and the first one after ablation (0.18 s). The boxes show the median and the upper and lower quartiles. Whiskers indicate the 5th and 95th percentile, while data points represent a single cut of one junction. Scale bar: 10 µm. All measurements were repeated in at least three independent experiments and performed on multiple WT/dKD clusters.

Because K_A^0 was previously found not to be independent of but scale with the fluidity β,[26] we plotted β against K_A^0 (Figure 3B). Interestingly, we found that the fluidity was not significantly different between WT and dKD cells (p = 0.53, with the same median of 0.6). However, we found a shift to larger K_A^0 values for WT cells compared with their dKD neighbors in co-culture. This increase can be attributed to the removal of excess surface area A_{ex} compared with the geometrical surface area A_0 of the cells via $K_A{}^0 = \widetilde{K}_A{}^0 \frac{A_0 + A_{ex}}{A_0}$.[27]

The picture which therefore emerges suggests that surface area is sacrificed to mitigate the external stress from adjacent dKD cells. This occurs at the expense of stiffening but preservation of fluidity. On one hand, we observed an unchanged fluidity and only a relatively small difference in prestress within the range of the standard deviation (0.49 ± 0.22 mN m^{-1} for WT cells compared with 0.31 ± 0.14 mN m^{-1} for dKD (median ± s.d.)). On the other hand, WT cells exhibited a substantially larger scaling factor K_A^0, with an increase of more than one order of magnitude (0.061 ± 0.084 mN m^{-1} for WT compared with 0.004 ± 0.016 N m^{-1} for neighboring dKD cells (median ± s.d.)). From K_A^0 we were able to estimate that about six-fold as much excess area was stored in dKD as in WT cells. This fits to the theoretical 5.7-fold surface area difference between the different cap geometries, indicating that the apical surface material is conserved upon

bioRxiv preprint doi: https://doi.org/10.1101/2022.05.23.492966; this version posted May 24, 2022. The copyright holder for this preprint (which was not certified by peer review) is the author/funder, who has granted bioRxiv a license to display the preprint in perpetuity. It is made available under aCC-BY-NC 4.0 International license.

stretching, i.e., dKD cells contract laterally and store the membrane/cortex apically, while WT cells sacrifice apical excess area. Although a tremendous amount of excess surface material is sacrificed by WT cells, the mechanics of the cortex is largely unaffected, with small differences in prestress. In agreement, we also did not observe an obvious change in the actin signal at the central cortex in Figure 2A (vide supra). In consequence, the observed lateral contraction of the dKD cells did not stem directly from their cortex but most likely from their perijunctional actomyosin ring (Figure 2A).

To test this and to characterize how the differential contractility translates into interfacial tension in the layer, we specifically examined the junctional tension using laser ablation, severing the cell junctions (Figure 3C-E). Particularly, we addressed the tensile properties of the cell junction between a WT and another WT cell, dKD/dKD junctions as well as the WT/dKD interface. In addition, we compared the new mechanical equilibrium in co-cultures with the junction tension in WT and dKD mono-cultures. To this end, we analyzed the recoil dynamics of the opposing vertex knots of the ablated junction over time (Figure 3D) and plotted the initial recoil velocity (Figure 3E).

We found a significant, four- to six-fold increase in recoil velocity for all junctions bordering a contractile dKD cell (10-12 µm s^{-1}, compared with 2-3 µm s^{-1} without any direct contact to a dKD cell). dKD/dKD junctions in co-culture were comparable with dKD mono-cultures ($p = 0.83$). Interestingly, the WT/dKD interface had slightly smaller recoil velocities than dKD/dKD junctions ($p = 0.29$), while WT/WT junctions displayed slightly but significantly higher velocities than WT mono-cultures. This highlights the establishment of a new mechanical equilibrium in co-cultures based on a tug-of-war between highly contractile dKD cells and compliant WT neighbors; in co-cultures, tension from dKD cells is accommodated by WT cells, while in dKD mono-cultures all cells exhibit increased tension. Overall, the data shows that the increased contractility of dKD cells indeed translates into increased junctional tension of all direct neighbors in the layer.

A further indication that the observed segregation in our study is based on interfacial tension, was another set of experiments in which we varied the mixing ratio between dKD and WT cells prior to seeding (Figure S2). We observed that the pattern of elongated dKD cell stripes which surrounded the predominately round WT clusters remained the same, independent of the mixing ratio. This is indicative of interfacial energy minimization according to the tension-based sorting hypothesis and in contrast to, e.g., demixing driven by active forces as reported recently.[13] It also supports the notion that the roundness of WT clusters was the consequence of the minimization of the interfacial contact region (and thereby interfacial tension) between WT cells and their dKD counterparts.

bioRxiv preprint doi: https://doi.org/10.1101/2022.05.23.492966; this version posted May 24, 2022. The copyright holder for this preprint (which was not certified by peer review) is the author/funder, who has granted bioRxiv a license to display the preprint in perpetuity. It is made available under aCC-BY-NC 4.0 International license.

Differential cell-cell adhesion of WT and dKD cells

While the increased contractility of dKD cells is well documented and could induce segregation via energy minimization, changes in intercellular adhesion might also be expected due to the loss of the adhesion-mediating junctional ZO proteins.

To quantify cell-cell adhesion, we performed AFM experiments with one cell attached to the AFM cantilever serving as the probe and the other one adhered onto the petri dish. The two cells were brought into conformal contact and separated after a short dwell in contact (Figure 4A). The separation forces between the two cells are not obtained under equilibrium conditions and are therefore referred to as the dynamic adhesion strength. We found decreased adhesion forces for all dKD cells (two dKD cells as well as a dKD adhering to a WT-GFP cell) as shown in Figure 4B. As a control we also compared WT cells and GFP-tagged WT cells. While the WT-GFP cells displayed slightly lower adhesion forces than pure WT cells, they are still consistently more adhesive than dKD cells ($p < 0.001$ compared with WT-GFP/dKD and $p < 0.01$ with dKD/dKD). Interestingly, the adhesion between two cells was always dominated by the respective weaker binding partner, i.e., the dKD cells, indicative of largely immobile receptor-ligand pairs. Accordingly, in WT/dKD co-cultures differential adhesion and contractility together determined the differential interfacial tension during cell segregation.

bioRxiv preprint doi: https://doi.org/10.1101/2022.05.23.492966; this version posted May 24, 2022. The copyright holder for this preprint (which was not certified by peer review) is the author/funder, who has granted bioRxiv a license to display the preprint in perpetuity. It is made available under aCC-BY-NC 4.0 International license.

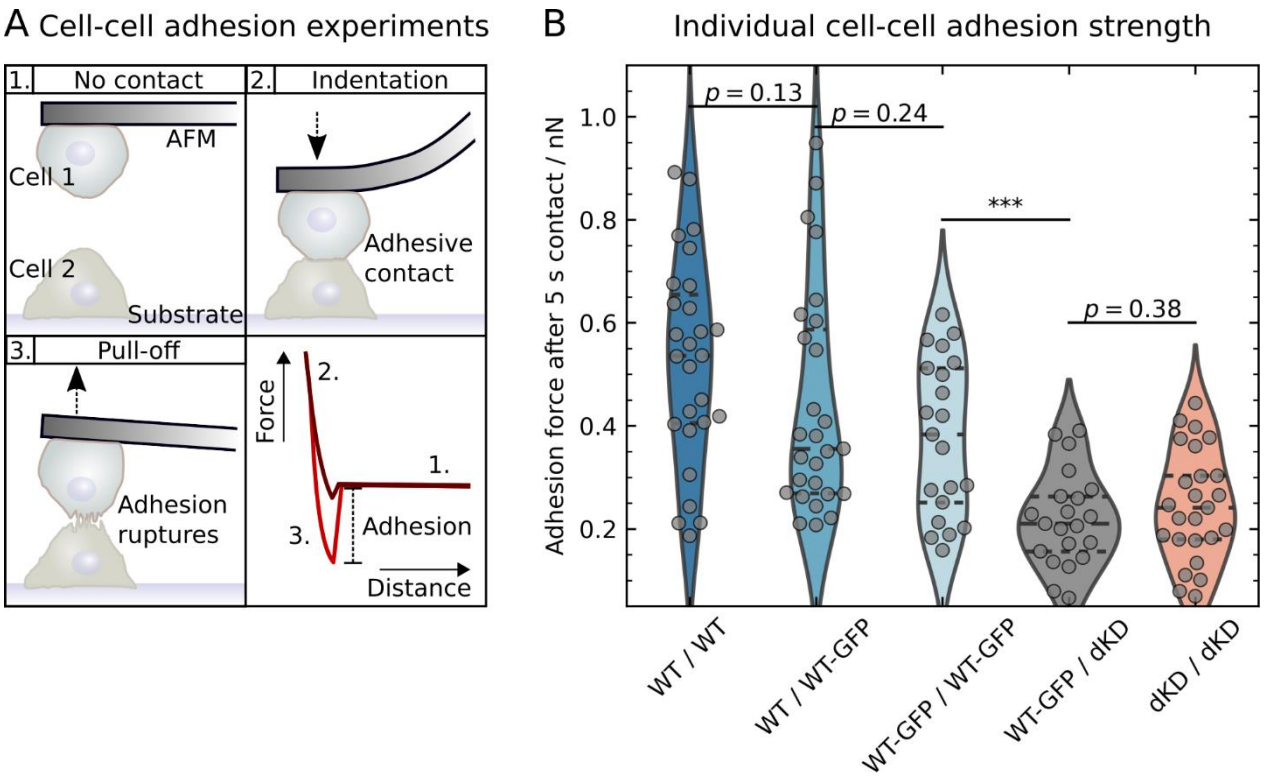

Figure 4. Differential intercellular adhesion of WT and dKD cells. A) AFM-based adhesion measurements: 1. Before or after an experiment, one cell is connected to the cantilever and one adheres to the culture dish substrate, without contact to each other. 2. Adhesive contact between cells is established at 2 nN for 5 s. 3. As the cantilever is retracted, the cells are pulled apart und bonds rupture. Schematic retraction curves depict small (dark red) and large (light red) adhesion forces. B) These adhesion forces are compared between different important cell combinations. Violins represent a kernel density estimation with horizontal, dashed lines showing the quartiles and median. Violins are scaled to have the same area. Single data points represent individual adhesion peak forces. Three consecutive indentation/retraction cycles were performed for each cell pair. For each combination, at least 4 individual cell-cantilever probes, and at least 8 cells on the substrate were measured, with experiments repeated on at least 4 days.

Time-scale dependency: Contractility drives early, adhesion final sorting

While we established that there is differential contractility and differential adhesion in WT/dKD co-cultures, it remains unclear, which one dominates over the other. Therefore, we performed the demixing experiments shown in Figure 1 again, however, this time in the presence of the Rho kinase (ROCK) inhibitor Y27632, in order to reduce cell contractility, switching off one of the contributions to demixing (Figure 5). This drug mainly affects the actomyosin contractility of cells, while the difference in cell-cell adhesion should remain the same.

bioRxiv preprint doi: https://doi.org/10.1101/2022.05.23.492966; this version posted May 24, 2022. The copyright holder for this preprint (which was not certified by peer review) is the author/funder, who has granted bioRxiv a license to display the preprint in perpetuity. It is made available under aCC-BY-NC 4.0 International license.

Upon first visual inspection after ROCK inhibition (Figure 5A), at early time stages no difference was discernible between the WT/dKD mixture and the WT/WT control. Only at later times, stronger demixing was observed in the WT/dKD co-culture as mirrored in the segregation index (Figure 5B1). Here, we plotted the untreated WT/dKD mixture from Figure 1, as a control, together with contractility-inhibited WT/dKD and WT/WT co-cultures. While the WT/WT control did not change its segregation behavior upon Y27632 administration, the very fast, early segregation of WT/dKD co-cultures (< 5 h) was prevented. Instead of this fast initial behavior, segregation of the WT/dKD mixture was slowed down. Nevertheless, after about 15 h the contractility-inhibited WT/dKD mixture reached approximately the same *SI* of approximately 0.7 as the untreated counterpart. Accordingly, the upregulated contractility of dKD cells was critical for early segregation, while the adhesion differential was still able to induce cellular demixing upon longer time scales.

As a control parameter, we also inspected the ratios of cell area and amount (Figure 5B2-3) as in Figure 1. The WT fraction of the cell amount (Figure 5B2) again served to provide context for the *SI* values and relative area coverage. While the untreated WT/dKD cell amount ratio was slightly shifted towards more WT cells, both drug-treated co-cultures remained at a 0.5 ratio (Figure 5B2). Interestingly, the proliferation in the WT/WT control was increased by Y27632 to the same level present in treated and untreated WT/dKD (except for the dKD extrusion after 15 h) as shown in Figure 5B2 and Figure S3A, while the *SI* remained much lower. To further rule out that local clustering due to proliferation dominates the segregation, we investigated the relationship between the *SI* and the cell amount (Figure S3A). The *SI* generally increased with increasing cell amounts but with a lower slope at higher cell amounts. However, while for both treated cultures and the WT/dKD mixture the proliferation rate was approximately constant over time, the scaling of the *SI* with the total cell amount was much different. At the same cell amount, the *SI* remained lower in the treated WT/WT control than in the untreated WT/dKD mixture. In addition, the difference in proliferation between the treated and untreated WT/WT samples did not translate into an increase in segregation. Note that the cell amount is essentially equivalent to cell density in our experiments because the size of the field of view was always the same. Together, while we cannot completely rule out an impact of proliferation, adhesion and contractility seemed to dominate the segregation.

To assess the cell contractility the area ratio once again served as a broad-scale readout (Figure 5B3). Here, we did observe the expected drop upon contractility inhibition for the WT/dKD mixture, while the WT/WT control was unaffected. Importantly, this drop in contractility remained over the whole duration of the experiments, confirming that the effect of the drug did not wear off over time.

bioRxiv preprint doi: https://doi.org/10.1101/2022.05.23.492966; this version posted May 24, 2022. The copyright holder for this preprint (which was not certified by peer review) is the author/funder, who has granted bioRxiv a license to display the preprint in perpetuity. It is made available under aCC-BY-NC 4.0 International license.

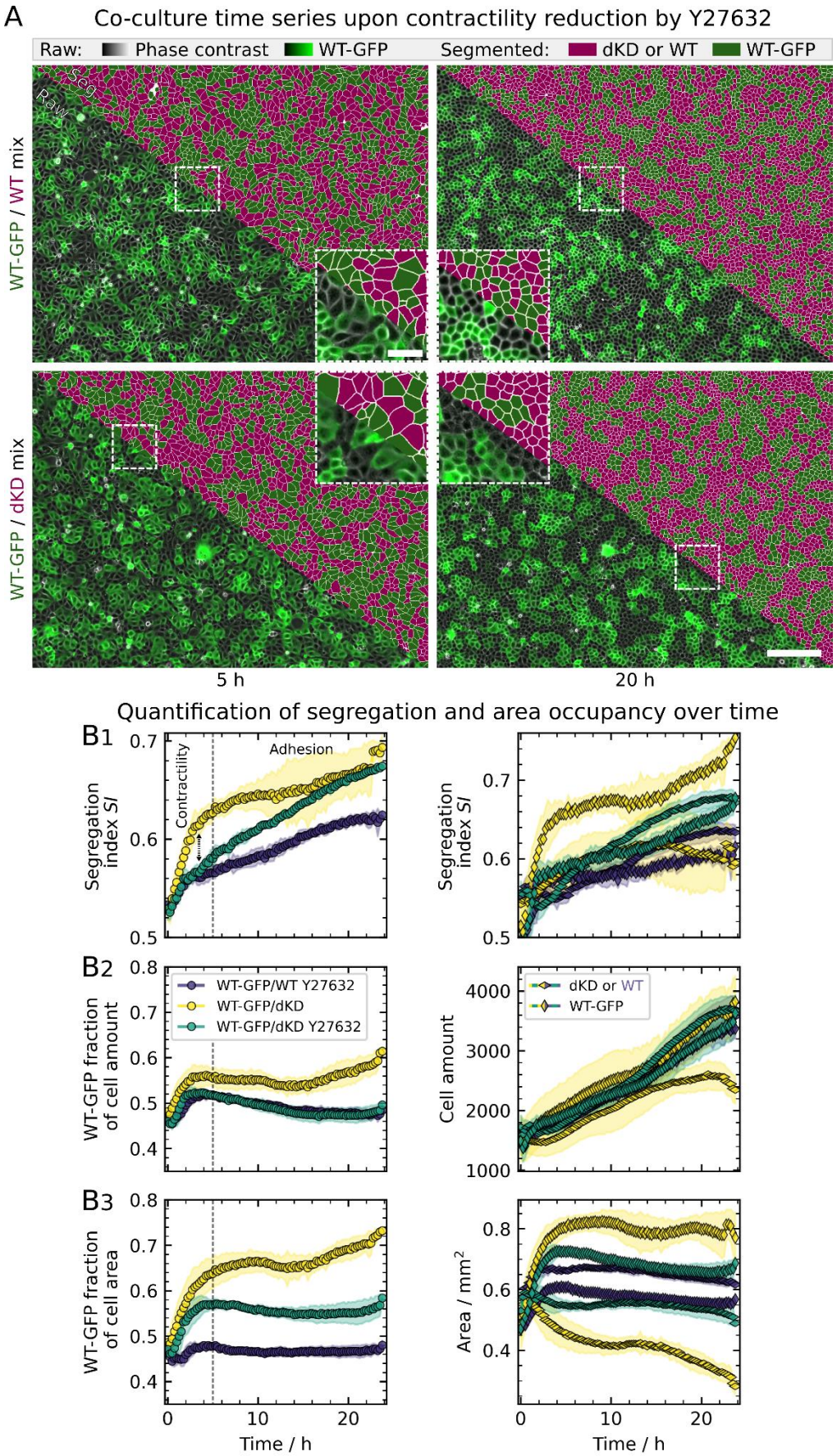

bioRxiv preprint doi: https://doi.org/10.1101/2022.05.23.492966; this version posted May 24, 2022. The copyright holder for this preprint (which was not certified by peer review) is the author/funder, who has granted bioRxiv a license to display the preprint in perpetuity. It is made available under aCC-BY-NC 4.0 International license.

Figure 5. Contractility drives early, adhesion final sorting. Demixing behavior of highly contractile dKD and wildtype cell co-cultures at an initial mixing ratio of 50:50, treated with 50 µm Y27632. Experiments and Figure panels are set up analogously to Figure 1, and, for comparison, untreated WT/dKD from Figure 1 was included. A) Example overlay of phase contrast (grayscale) and fluorescence (green: WT-GFP cells) channels with corresponding segmentations (green: WT-GFP, magenta: dKD cells in WT-GFP/dKD mix or WT in WT-GFP/WT control, respectively). Samples were imaged immediately after seeding and mounting on the microscope (0 h). Scale bars: 200 µm and 50 µm (zoom-in). B) Demixing, cell amount, and area occupancy quantification. The vertical dashed line at 5 h indicates two distinct demixing time scales, thought to be determined by contractility and adhesion. B1) The segregation index *SI*, defined as the average ratio of homotypic and all cell neighbors, quantifies the demixing degree. The *SI* is shown averaged over both cell types (left) as well as separately for each cell type (right). B2) Left: Relative cell amount, calculated as the ratio of the amount of WT-GFP cells and the total cell amount. Right: Total cell amounts of each cell type. B3) Left: WT-GFP fraction of the overall cell area, calculated as the ratio of the WT-GFP area and the total cell area, indicating contractility discrepancies between the cell types. Right: Total covered area of each cell type. Corresponding velocity and persistence analyses can be found in Figure S3. Means and standard deviations are shown. 6 separate regions from 3 culture dishes (two per dish), acquired on separate days, were measured and are shown per co-culture mix.

To rule out that the drug acts on cell motility (e.g., due effects on the focal adhesions on the substrate) influencing demixing, we quantified the velocity and persistence via cell tracking (Figure S3B). We investigated this particularly for the first 5 h, where the impact of the drug on segregation is the strongest. If higher motility actually was a driving factor for random mixing, we would expect an increase in the motility parameters particularly of the WT/dKD mixture upon drug treatment. However, this was not the case, but, to the contrary, the motility parameters even decreased slightly or remained the same (Figure S3B). The WT/WT control showed a slight drop in both parameters, while its (de-) mixing behavior was largely unaffected. Accordingly, the drug provoked the delay in WT/dKD sorting not by affecting motility but indeed via inhibiting cellular contractility.

Together, data of this experiment showed that co-cultures can display an intricate interplay of contractility and adhesion driving cell segregation on distinct time scales.

Discussion

Our goal was to scrutinize the driving force for demixing of co-cultures consisting of WT and dKD MDCKII cells displaying both different adhesion due to knock down of ZO1/2 and differential contractility due to actomyosin upregulation. We found that the main driving forces for creating

bioRxiv preprint doi: https://doi.org/10.1101/2022.05.23.492966; this version posted May 24, 2022. The copyright holder for this preprint (which was not certified by peer review) is the author/funder, who has granted bioRxiv a license to display the preprint in perpetuity. It is made available under aCC-BY-NC 4.0 International license.

clusters of dKD cells coexisting with WT clusters are time scale separated. On short time scales (within the first five hours) differential contractility prevails, while on longer times scales (>5 h) cell sorting is driven predominately by differential adhesion. To our knowledge, this is the first time that a separation of time scales in cellular segregation is described and attributed to distinct mechanical properties. Our data suggest that if differential contractility is abolished, differential adhesion alone is sufficient for cell demixing, but less efficient.

The envisioned mechanism comprising adhesion- and contractility-based cell segregation is summarized in Figure 6: while in randomly mixed WT cultures adhesion between all cells is the same and they display similar contractility, in WT/dKD co-cultures the adhesion and contractility between the cell types are considerably different, inducing segregation into clusters. In response to the contraction of adjacent dKD neighbors, WT cells are stretched and sacrifice excess surface area. If contractility is balanced again by pharmacological intervention, segregation based on differential contractility is strongly delayed. However, upon longer time scales the remaining adhesion differential still induces the same amount of segregation as in untreated layers, highlighting a redundant but time-dependent role of contractility and adhesion. Considering that adhesion complexes mature progressively over time,[28] whereas contractility is a property of individual cells, it makes sense that differential contractility promotes sorting immediately while adhesion acts on longer time scales.

It is well established that tight junction-depleted cells show increased contractility.[29–34] However, the implications of increased contractility of dKD cells for the behavior of the monolayer was only studied with emphasis on impaired migration dynamics and signaling.[23,24] Here, we showed that epithelial cells which are stretched by their contractile neighbors respond primarily by apical area dilatation, instead of by cortex mechanics adaptation. We were able to quantify a six-fold excess area difference between the stretched WT and the constricted dKD cells, equivalent to the change in geometric surface area, indicating the conservation of excess material instead of its recycling. This seems reasonable for co-cultures as well as dKD mono-cultures, which were described previously, where two populations emerged in a tug of war: a contractile population that stretches out the neighboring cell population.[23] However, in that work it remained unclear if excess membrane area dilatation indeed dominates the stretch response. During development a generation of two mechanical cell populations among the same cell type was in fact identified as an emergent property upon collective cell interactions.[35] A recent study implicated asymmetric ROCK signaling in inducing these two populations interacting in confluent dKD mono-cultures.[24] This tug of war might intuitively favor a segregation into clusters in order to decrease the number of WT cells that is stretched by adjacent dKD neighbors.

bioRxiv preprint doi: https://doi.org/10.1101/2022.05.23.492966; this version posted May 24, 2022. The copyright holder for this preprint (which was not certified by peer review) is the author/funder, who has granted bioRxiv a license to display the preprint in perpetuity. It is made available under aCC-BY-NC 4.0 International license.

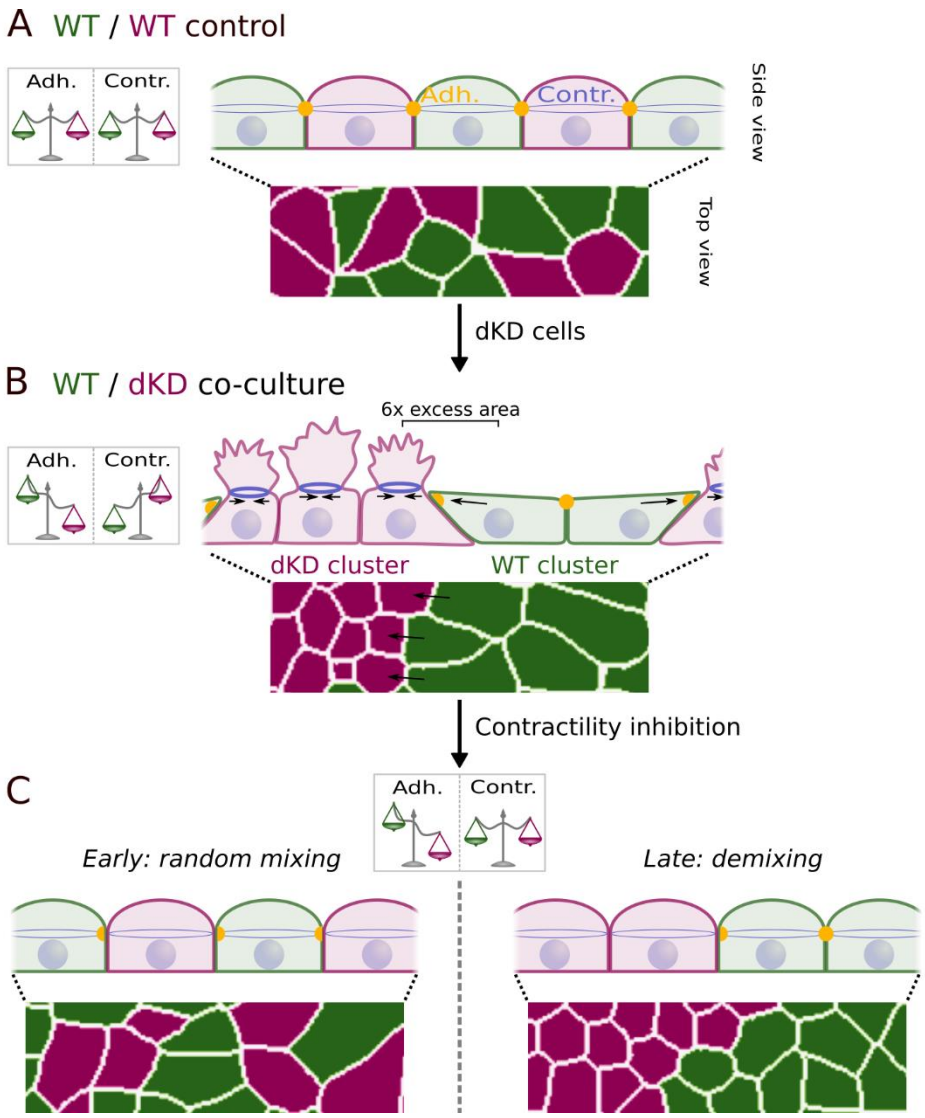

Figure 6. Proposed model of the interplay between adhesion and contractility in WT/dKD cell layers. A) In WT/WT control layers, adhesion is the same between all cells and they are equally contractile, hence, random mixing takes place. B) Adding dKD cells induces differences in both adhesion and contractility between the cell types. dKD cells lose some adhesive contact and contract excessively, yielding tremendous apical excess surface area. As a consequence, neighboring WT cells are stretched out and respond by surface area dilatation. C) To test the relative impact of adhesion and contractility, the latter was balanced again by drug addition, revealing a temporal dependency: balanced contractility restores random mixing at early stages but differential adhesion is still able to promote cell sorting into clusters on long time scales.

Our study confirms that segregation can be fostered by differential interfacial tension, however, we identified a stronger contribution from differential adhesion than contractility. On the one hand, adhesion-based sorting was shown before to emerge in cell cultures, e.g., upon different expression levels of cadherins.[6,36–38] Similarly, sorting based on cadherin levels was demonstrated

bioRxiv preprint doi: https://doi.org/10.1101/2022.05.23.492966; this version posted May 24, 2022. The copyright holder for this preprint (which was not certified by peer review) is the author/funder, who has granted bioRxiv a license to display the preprint in perpetuity. It is made available under aCC-BY-NC 4.0 International license.

in follicle and retina cells of Drosophila oocytes.[39,40] Signaling-controlled cadherin turnover has also been implicated in cell segregation.[41,42] Note, in our study, adhesion differences were induced by tight junction disruption, which was also shown by previous work to decrease adhesion strength, in agreement with our data.[43] Purely adhesion-based sorting was recently confirmed via simulations and experiments in direct relation to constant contractility.[18] On the other hand, differential contractility was found to aid sorting in an embryo and possibly dominate over adhesion.[44,45] In co-cultures of zebrafish germ layer cells, differential contractility alone was found to be sufficient for sorting.[44] However, while sorting also took place on two time scales, a fast, early (< 0.5 h) and a slower, later time scale, the authors did not investigate the temporal evolution further. An interplay between adhesion and contractility was confirmed in recent studies using vertex/Voronoi models.[9,15,16] In particular, interfacial tension was shown to be determined by the ratio of cell adhesion and contractility, governing the tissue-scale tension.[9] Accordingly, the increased contractility paired with the lower adhesion of dKD cells translates well into the high tension values measured by laser ablation.

However, a demixing mechanism of locally increased contractility at the boundary between two cell types, as reported in Drosophila wing discs, can be ruled out in our work.[10–12] While we measured tremendous differences in line tension between the different cell types, the WT/dKD interface did not exhibit the highest tension but rather values equal or slightly below that of dKD/dKD junctions.

Another mechanism in contrast to our data was proposed by a recent study examining the demixing of E-cadherin-depleted and wildtype MDCK cells. The authors identified active cell forces as the governing factor of sorting.[13] While the demixing behavior in that study appears very similar to our data, the initial segregation was slower. Furthermore, they observed a pattern reversal at uneven mixing ratios which was absent in our co-cultures. This stability of the sorting pattern is indicative of interfacial energy minimization by minimizing the contact region between heterotypic cell types upon sorting, based on adhesion and/or contractility.[13] E-cadherin-depleted and wildtype keratinocytes were recently shown to sort mainly based on shape disparities and this was thoroughly explained in vertex simulations as well as observed earlier in zebrafish embryos.[14,46] While in our cell lines shape differences seem to be small, we cannot rule out their contribution.[23] Although, similarly to the area disparities, both parameters are probably only a consequence of the tremendous tension differential with stretched WT and laterally constricted and therefore rounded dKD cells.

bioRxiv preprint doi: https://doi.org/10.1101/2022.05.23.492966; this version posted May 24, 2022. The copyright holder for this preprint (which was not certified by peer review) is the author/funder, who has granted bioRxiv a license to display the preprint in perpetuity. It is made available under aCC-BY-NC 4.0 International license.

One limitation of our study, similar to most fundamental demixing experiments, is the possible crosstalk of contractility and adhesion.[47] For instance, actomyosin contractility has been shown to enhance adherens junction-based adhesion.[48–50] Accordingly, our Y27632 experiments might not only have reduced contractility but also adhesion. However, there would still be the disruption of the tight junctions in dKD cells. In addition, if the adhesion difference had been just as abolished as the differential contractility, we would not have observed the prevailing demixing at longer time scales. Actomyosin contractility has also been shown to modulate focal adhesions and thereby cell motility.[51–53] However, we observed no influence of motility on sorting, possibly due to the high cell density in our experiments (with confluence reached after only a few hours).

In addition, cell sorting could be influenced by proliferation creating local clusters. However, upon Y27632 treatment the WT/WT control increased its proliferation to the same level present in treated and untreated WT/dKD mixtures, yet, its *SI* remained much lower. At the same cell amount, the *SI* remained lower in the treated WT/WT control than in the untreated WT/dKD mixture. In addition, the large difference in proliferation between the treated and untreated WT/WT samples did not translate into an increase in segregation. The cell amount ratio of the cell types was also consistent among the WT/dKD mixture and its respective WT/WT counterpart, both treated and untreated, whereas their *SI* differed. Together, while we cannot completely rule out an impact of proliferation, contractility and adhesion seem to dominate the segregation.

Another caveat to note is that due to technical limitations, our cell adhesion measurements are on much shorter timescales than the observed mixing dynamics and the relevant cell-cell interactions in general.[54] Nevertheless, in agreement with other work, it is reasonable to assume that the loss of tight junction integrity reduces intercellular adhesion on all relevant timescales.[43]

In general, the presented model system has the advantage of great experimental accessibility compared with in vivo experiments but lacks some physiological conditions, e.g., properties of the substrate. While the cell-substrate adhesion might be different, it is well suited to capture the general physics of cell-cell interactions that also governs sorting in vivo. Along this line, previous work successfully compared consistent in vivo and in vitro tension-based cell sorting experiments.[44,45]

Ultimately, our data suggest that adhesion alone is sufficient, but less efficient in driving cell sorting without differential contractility. This could yet be another example of how biology employs functional redundancy to ensure fundamental processes such as sorting of different cell types.

bioRxiv preprint doi: https://doi.org/10.1101/2022.05.23.492966; this version posted May 24, 2022. The copyright holder for this preprint (which was not certified by peer review) is the author/funder, who has granted bioRxiv a license to display the preprint in perpetuity. It is made available under aCC-BY-NC 4.0 International license.

Material and Methods

Cell culture handling

Madin-Darby Canine Kidney cells (strain II, MDCKII; European Collection of Authenticated Cell Cultures, Salisbury, UK) were cultured at 37°C and 5% CO_2, under humid conditions, and in minimum essential medium (Life Technologies, Paisley, UK) containing Earle's salts, 2 mM GlutaMAX (ThermoFisher Scientific, Waltham, Massachusetts, USA), 2.2 g L^{-1} $NaHCO_3$, and 10% fetal bovine serum (BioWest, Nuaillé, France), here termed $M10F^-$. The cells were passaged two to three times per week before reaching confluence with phosphate buffered saline pH 7.4 (PBS; Biochrom, Berlin, Germany) containing trypsin/EDTA (0.25%/0.02% w/v; BioWest/Biochrom).

Genetic generation of cell lines

ZO1/2 knockdown was effected by Beutel et al. using Crispr/Cas.[55] WT-GFP cells were created as described in Skamrahl et al.[23] Clones of MDCKII cells expressing GFP-myosin-2-A were generated by transfecting cells with pTRA-GFP-NMCH II-A plasmid (Addgene plasmid # 10844). Clones expressing the GFP tag in a stable manner were selected via Neomycin resistance (G418). Upon selection, the cell pool was sorted using FACS to enrich cells with GFP at a moderate level. For N-terminal endogenous labeling of myosin with mNeon in dKD cells, the myosin-2-A exon was targeted using Crispr/Cas. MDCKII WT-ZO1-mNeonGreen cells were generated by Beutel et al. targeting the initial ZO1 exon with Crispr/Cas.[55]

Cell seeding and demixing experiments

Petri dishes (35 mm, ibiTreat 1.5 polymer cover slip; ibidi, Martinsried, Germany) were used. Cells were trypsinized and mixed well before being seeded to ensure an initially random distribution.

Two sets of seeding conditions were used: In *seeding approach one*, cells were seeded at 6 10^5 cells in 1 mL $M10F^-$, rinsed after about 5 h with $M10F^-$, supplied with sufficient $M10F^-$ (2-3 mL), and then imaged over time or fixed/measured after 28 h or 48 h. These conditions were used for experiments in Figure 2 and 3. Because in the first experimental approach the initial demixing dynamics were missed and the cells were still subconfluent for a long time (while the image quality was slightly better due to the rinsing step and the lower cell density), we changed the experiment: Cells were seeded at 1.2 10^6 cells in 1 mL $M10F^-$ and imaged immediately. This *second seeding approach* was used for the main demixing experiments in Figure 1, 5 and S1-3. To reduce cellular

bioRxiv preprint doi: https://doi.org/10.1101/2022.05.23.492966; this version posted May 24, 2022. The copyright holder for this preprint (which was not certified by peer review) is the author/funder, who has granted bioRxiv a license to display the preprint in perpetuity. It is made available under aCC-BY-NC 4.0 International license.

contractility, the same second set of experiments was performed with Y27632 ("InSolution" Y27632; Sigma-Aldrich, Steinheim, Germany) added to the mixed cell solution, to reach the desired final concentration, immediately before seeding. Importantly, the cell behavior (*SI*, cell area ratio, number ratio as well as morphology) was comparable between both seeding conditions.

For imaging, cells were placed into the incubation system of a fully automated inverted light microscope (BZ-X810; Keyence, Neu-Isenburg, Germany) equipped with a 10X phase contrast objective (Nikon CFI60 Series; Keyence). The temperature was calibrated to be 37°C at the cells using a local temperature probe (Testo 735; Testo, Lenzkirch, Germany), 5% partial CO_2 pressure was set, and sufficient humidity was ensured with distilled water in the appliance of the incubation system as described before.[23] Phase contrast images were recorded at 1 frame per 7.5 min, 14 bit, 25% illumination power, exposure times of 1/25 s, and without binning, zoom, or gain, yielding a field of view of 1920 x 1440 pixels (1449.6 µm x 1087.2 µm). Corresponding fluorescence images for each frame were recorded at low light exposure to prevent phototoxicity. For this, we used 40% illumination power, 3.5 s exposure and 4X gain, without binning to allow direct overlay of both channels. In between frames, all light exposure was turned off. Focus tracking was applied and three vertical slices were chosen in a range of 10 µm (5 µm pitch) to avoid drift effects. For the manuscript figures, images were brightness-adjusted in Fiji to improve visibility,[56] particularly in relation to the phase contrast. The fluorescence brightness was typically increased (images were relatively dark due to the low-exposure settings).

Automated cellular segmentation

Cell segmentation was performed as described in Skamrahl et al.[23] using Cellpose 1.0[57] in conjunction with python-based parallel processing. Raw phase contrast or fluorescence images were directly used as input. To optimize cell recognition, the following parameters were used: For the phase contrast channel, the flow and cell probability thresholds were set to 1 and -6, respectively. For the fluorescence channel, the flow and cell probability thresholds were set to 0.9 and -5, respectively.

Further automated analysis of cell parameters

To calculate cell parameters such as the x- and y-position, area, and aspect ratio, OpenCV was used as described in Skamrahl et al.[23,58,59] Note that OpenCV might omit a small amount of cells present in the Cellpose data, for example due to a failed aspect ratio calculation (e.g., due to a

bioRxiv preprint doi: https://doi.org/10.1101/2022.05.23.492966; this version posted May 24, 2022. The copyright holder for this preprint (which was not certified by peer review) is the author/funder, who has granted bioRxiv a license to display the preprint in perpetuity. It is made available under aCC-BY-NC 4.0 International license.

falsely recognized particle which is only a few pixels in size). Therefore, to ensure correct cell indexing between Cellpose and OpenCV in all functions, we used the contours (and masks) from OpenCV for all following operations. For cell tracking, Trackpy[60] was used to link the cell positions from OpenCV. The link function was used with a memory of 3 frames and 6.04 µm (8 pixels) as the maximal displacement. Trajectories shorter than 5 frames were discarded. Drift correction was not necessary.

Automated cell type recognition, neighbor analysis, and segregation index calculation

Using the masks generated by Cellpose, three main steps were performed in python. To identify the cell type (WT-GFP or unlabeled WT in WT-GFP/WT, WT-GFP or unlabeled dKD in WT-GFP/dKD mixes), the mask returned by Cellpose for the fluorescence and phase contrast channel were compared. In the masks, all pixel values belonging to one cell body correspond to the respective cell index with the background being zero. We iterated over the masks in the phase contrast channel and evaluated the modal value of the respective cell pixels in the fluorescence channel. If the modal value of the respective cell pixels corresponded to zero in the fluorescence channel (i.e., background without a cell), the cell was assigned as unlabeled. If the modal value was greater than zero, it was assigned as WT-GFP. The cell types were assigned in the phase contrast masks to finally yield a complete set of all cells for each image. Next, nearest neighbor analysis was performed to find direct neighbors. For each cell, an OpenCV line scan was performed between the center of this cell and each surrounding cell. All zeros, the own cell index, and the index of the respective neighbor were removed from the line. Only if no values remained in the line, i.e., no other cell index was crossed, the two cells were assigned as neighbors. This was restricted to a window of 50 pixels x 50 pixels (37.75 µm x 37.75 µm) around each cell to prevent extremely high computation times and also false neighbor assignment of cells that are separated by empty space in the early, not fully confluent state. Neighbor assignments were noted as ones in a so-called adjacency matrix, in which the column (or row) number corresponds to the cell index, the rest of this symmetric matrix was filled with zeros. Lastly, the number of neighbors of each cell in the image was the sum of all ones in the respective column (or row) in the matrix. We distinguished the number of homotypic neighbors by only summing over the positions in the matrix given by the cell assignments. Per definition, the segregation index *SI* was the ratio of the homotypic and all neighbors for each cell. Finally, to generate the plots, the *SI* was averaged over all cells or separately over all cells of each cell type.

bioRxiv preprint doi: https://doi.org/10.1101/2022.05.23.492966; this version posted May 24, 2022. The copyright holder for this preprint (which was not certified by peer review) is the author/funder, who has granted bioRxiv a license to display the preprint in perpetuity. It is made available under aCC-BY-NC 4.0 International license.

Cell labeling and confocal fluorescence microscopy

For the depicted confocal images, 6 10^5 cells in 1 mL were seeded (first seeding approach, vide supra) and fixed after 28 h or 48 h. Before labeling, samples were incubated for 20 min with a paraformaldehyde/glutaraldehyde solution (4% (w/v) / 0.1% (w/v) in PBS; Science Services, Munich, Germany / Sigma-Aldrich). Cells were incubated for 5 min in Triton X-100 (0.1% (v/v) in PBS) to permeabilize the plasma membrane. After rinsing three times with PBS, samples were incubated in blocking/dilution buffer (PBS containing 2% (w/v) bovine serum albumin and 0.1% (v/v) Tween20) for 30 min to block unspecific binding sites.

Samples were incubated in primary antibody diluted in blocking/dilution buffer for 1 h using the following reagents. Phospho-myosin: 2 µg mL^{-1} (1:200) light chain 2 (Ser 19) rabbit IgG1 (Cell Signaling Technology, Danvers, Massachusetts, USA), ZO1: 5 µg mL^{-1} (1:100) mouse ZO1-1A12 IgG1 AlexaFluor 488 (Invitrogen, ThermoFisher Scientific, Waltham, Massachusetts, USA). After incubation with the primary antibody, samples were briefly rinsed with PBS. Next, they were washed with PBS, with 0.1% (v/v) Triton X-100 in PBS, and again with PBS, each for 5 min on a shaking plate (75 rpm).

The secondary antibody (AlexaFluor 546-conjugated goat anti-rabbit IgG; Life Technologies, Carlsbad, USA) was diluted with blocking/dilution buffer to a concentration of 5 µg mL^{-1}. Actin labeling was performed using 165 nM AlexaFluor 647-phalloidin (Invitrogen), incubated and diluted together with the secondary antibody. The incubation time was 1 h. Following the secondary antibody, samples were washed three times with PBS for 5 min each on a shaker (75 rpm).

Nucleus staining was performed by a 15 min-incubation with DAPI (Sigma-Aldrich), diluted to 50 ng mL^{-1}. Before imaging, the cells were rinsed with PBS three times and then kept in PBS. Labeling and microscopy were performed at room temperature.

For fluorescence imaging experiments a confocal laser scanning microscope (FluoView1200; Olympus, Tokyo, Japan) was used with a 60X objective (oil immersion, *NA* = 1.25). Image processing (3D representations, z-projections, color choice, and overlay) and brightness adjustment were performed in Fiji.[56] For the figures, brightness usually had to be slightly increased due to low-bleaching acquisition settings.

bioRxiv preprint doi: https://doi.org/10.1101/2022.05.23.492966; this version posted May 24, 2022. The copyright holder for this preprint (which was not certified by peer review) is the author/funder, who has granted bioRxiv a license to display the preprint in perpetuity. It is made available under aCC-BY-NC 4.0 International license.

AFM imaging

Two days after seeding at 6 10^5 cells in 1 mL (first seeding approach), cells were rinsed once with PBS containing 0.1 g L^{-1} Mg^{2+} and 0.133 g L^{-1} Ca^{2+} (PBS^{++}; Sigma-Aldrich) and incubated with glutaraldehyde solution (2.5% (v/v) in PBS^{++}) for 20 min. PBS^{++} was used instead of PBS without magnesium and calcium ions, because the dKD cell layers were more susceptible to dissolution of ion-dependent adhesion sites due to the impaired diffusion barrier function. Prior to AFM imaging, samples were rinsed three times to remove residual glutaraldehyde. A NanoWizard 4XP AFM (Bruker Nano, JPK, Berlin, Germany) was used for imaging. The AFM was mounted on an inverted light microscope (IX 83; Olympus) to allow visual inspection via phase contrast and cell recognition via fluorescence. Imaging was carried out in contact mode with MLCT C cantilevers (Bruker AFM Probes, Camarillo, USA) in PBS with a line scan rate of 0.18 Hz translating to a velocity of 40 µm s^{-1}, a force of 0.14 nN, and a pixel size of 50 nm. The IGain was set to 20 Hz and the PGain was 0.002. The AFM was calibrated as described below, in a small area at the edge of the dish where a few cells were scratched off. Height and error images were obtained from the manufacturer's SPM Data Processing software (JPK, Berlin, Germany) upon standard linear plane correction (to correct for a slight tilt of the petri dish surface) without further processing.

AFM indentation and force relaxation measurements

Force indentation-relaxation experiments were performed using a NanoWizard 4XP AFM (Bruker Nano) with a 37°C-heated stage (JPK) mounted on an inverted microscope (IX 83; Olympus) using silicon nitride cantilevers with a nominal spring constant of 0.01 N m^{-1} (MLCT C; Bruker AFM Probes). Prior to experimentation, cantilevers were rinsed with isopropanol and PBS and functionalized by incubation for 1 h with fluorescein isothiocyanate-conjugated Concanavalin A (2.5 mg mL^{-1} in PBS; Sigma-Aldrich).

The sensitivity of the AFM was determined by recording force curves on bare substrate and the spring constant of each cantilever was determined by the thermal noise method.[61] To allow the co-culture system to fully establish its differential collective mechanics, we allowed 2 days before measuring (with the first seeding approach). Cells were rinsed three times with $M10F^-$ containing 0.2 mg mL^{-1} Penicillin (Biochrom), 0.2 mg mL^{-1} Streptomycin (Biochrom), and 15 mM HEPES ($M10F^+$; BioWest).

Before the experiments, 2.5 mL $M10F^+$ was supplied to the cells and the temperature was set to 37°C. The cells were indented at a constant speed of 2 µm s^{-1} to a maximum force of 1 nN. After

bioRxiv preprint doi: https://doi.org/10.1101/2022.05.23.492966; this version posted May 24, 2022. The copyright holder for this preprint (which was not certified by peer review) is the author/funder, who has granted bioRxiv a license to display the preprint in perpetuity. It is made available under aCC-BY-NC 4.0 International license.

a dwell time of 1 s at constant height the indenter was retracted at the same speed. Maps were recorded at a lateral scan resolution of 2 µm per pixel with one indentation-relaxation cycle each. Furthermore, five consecutive force curves at the center of individual cells in the monolayer were measured with the same parameters. For the data in Figure 3B the individual curves at the cell center were pooled with curves at the cell center from the maps.

Force curve fitting and viscoelastic model

Indentation-relaxation curves of the cell center were analyzed as described recently[23] using the viscoelastic theory introduced by Cordes et al.[26] Briefly, the cell surface was described as a spherical cap. In this model the cell is considered as a liquid-filled object surrounded by a thin isotropic viscoelastic shell, which is deformed at constant volume. The force F acting on the apical cortex is given by:

$$F = 2\pi \left({R_1}^2 \left(\frac{R_1 \sin\phi + r_1 \sin\theta}{{R_1}^2 - {r_1}^2} \right) - R_1 \sin\phi \right) T(t)$$

with the radius R_1 at the base of the spherical cap and the contact angle ϕ upon deformation. r_1 is the contact radius with the conical indenter, $\theta = \frac{\pi}{2} - \vartheta$ with ϑ, the cone half angle.

Viscoelasticity of the shell is included in the tension term $T(t)$ through a time t dependent area compressibility modulus $K_A = {K_A}^0 (t/t_0)^{-\beta}$ with the scaling parameter ${K_A}^0$ and $t_0 = 1$ s (set arbitrarily). Now, a set of nonlinear equations for the shape of the deformed cell is solved to fulfill force balance and the boundary condition of constant volume. The resulting shapes are minimal surfaces to minimize the stretching energy. The average geometry was derived via AFM imaging, confocal microscopy, and AFM-combined phase contrast and fluorescence: for WT cells a radius of 12 µm and an initial cap angle of 15° were used, while in case of dKDs R_1 = 5 µm and an angle of 25° was used. Cells were chosen close to the WT/dKD interface to most closely compare the mechanical differential. The difference in excess area A_{ex} between cell types was calculated via the correction factor ${K_A}^0 \frac{A_0 + A_{ex}}{A_0}$ with the surface area A_0 of the cell cap as first described in a study comparing isolated membranes and epithelial cells.[27]

bioRxiv preprint doi: https://doi.org/10.1101/2022.05.23.492966; this version posted May 24, 2022. The copyright holder for this preprint (which was not certified by peer review) is the author/funder, who has granted bioRxiv a license to display the preprint in perpetuity. It is made available under aCC-BY-NC 4.0 International license.

Self-written Python scripts in conjunction with the JPK SPM Data Processing software were used for the analysis. A linear fit prior to the contact point was applied to correct the baseline. JPK SPM Data Processing was used to determine the contact point. Poorly fitted Curves, e.g., yielding non-physical (negative) parameters, were discarded.

Laser ablation

Laser ablation was performed on a Zeiss LSM 780 NLO system driven by Zen Black software version 11.00. Image pixel size was 0.268 µm x 0.268 µm. The objective used was a Zeiss C-Apochromat 40X/1.2 W. Ablation was performed with an 800 nm Titanium/Saphire femtosecond pulsed laser Chameleon from Coherent (Santa Clara, USA) with a power of 3.2 W at the laser head, 60% laser output set in Zen Black, reflected by MBS 760+, with pixel dwell time for photomanipulation of 7.2 µs, single iteration, ablation area was line scan, 10 pixels. For measuring the recoil velocity, the lateral membrane of MDCK WT and MDCK ZO1/2 dKD cells was highlighted by ZO1-mNeonGreen and myosin-2-A-mNeon, respectively, with the following settings: mNeonGreen was excited with 488 nm (Argon Laser) with MBS 488/561/633, emission filter used was 490-570 nm, pixel dwell time 2.83 µs, approximately 7.7 fps with GaAsP detector. Allowing the cell layer to fully establish its mechanics, laser ablation was performed after 2 days of growth (first seeding approach).

Cell-cell adhesion measurements

All cell-cell adhesion measurements were carried out using a Cellhesion 200 AFM (JPK). The AFM was mounted on an optical IX 83 microscope (Olympus) to allow identification of GFP-tagged and unlabeled cells. Experiments were performed immediately after seeding. Prior, tip-less cantilevers (MLCT-O10 B; Bruker AFM Probes) were rinsed several times with distilled water and isopropanol and then treated with poly-D-lysine hydrobromide (0.1 mg mL^{-1} in water, Sigma-Aldrich) for two days. A cell was picked and centered as well as possible above a cell on the substrate. Indentation was performed to a force of 2 nN, and a dwell of 5 s at constant height was chosen. The approach and retract velocity was set to 0.5 µm s^{-1}. The experiments were restricted to 2 h per day to avoid proliferation and advancing adhesion, which could interfere with the measurements. The adhesion peak force was determined using the JPK Data Processing software after linear baseline correction and contact point detection.

bioRxiv preprint doi: https://doi.org/10.1101/2022.05.23.492966; this version posted May 24, 2022. The copyright holder for this preprint (which was not certified by peer review) is the author/funder, who has granted bioRxiv a license to display the preprint in perpetuity. It is made available under aCC-BY-NC 4.0 International license.

Statistical analysis and reproducibility

The cell behavior was very reproducible between different samples as well as among seeding conditions. Significance of the AFM indentation data in Figure 3 was tested using the Mann-Whitney U test. The laser ablation data in Figure 3 and the cell-cell adhesion forces in Figure 4 were tested using Welch's t-test. All statistical analyses were performed in Python.
A p value of < 0.05 was considered significant and denoted by one asterisk (*). $p < 0.01$ and $p < 0.001$ were indicated by two (**) and three (***) asterisks, respectively.

Acknowledgements

Funding from the DFG grants SPP1782 and DFG JA963/19-1 is gratefully acknowledged. We thank Tabea A. Oswald, Burkhard Geil, and Jonathan F.E. Bodenschatz for helpful discussions. M.S., J.S., M.M., J.G., and A.R. performed experiments and analyzed data. M.S. and M.F. developed analyses. A.H. and A.J. initiated and supervised the research. M.S. wrote the manuscript with the help of A.J. All authors helped with discussions and careful proofreading.

Conflict of interest

There is no conflict of interest to declare.

References

1. Fagotto, F. The cellular basis of tissue separation. *Development* **141**, 3303–3318 (2014).
2. Heisenberg, C.-P. & Bellaïche, Y. Forces in Tissue Morphogenesis and Patterning. *Cell* **153**, 948–962 (2013).
3. Moscona, A. & Moscona, H. The dissociation and aggregation of cells from organ rudiments of the early chick embryo. *J. Anat.* **86**, 287–301 (1952).
4. Townes, P. L. & Holtfreter, J. Directed movements and selective adhesion of embryonic amphibian cells. *J. Exp. Zool.* **128**, 53–120 (1955).
5. Steinberg, M. S. Does differential adhesion govern self-assembly processes in histogenesis? Equilibrium configurations and the emergence of a hierarchy among populations of embryonic cells. *J. Exp. Zool.* **173**, 395–433 (1970).

bioRxiv preprint doi: https://doi.org/10.1101/2022.05.23.492966; this version posted May 24, 2022. The copyright holder for this preprint (which was not certified by peer review) is the author/funder, who has granted bioRxiv a license to display the preprint in perpetuity. It is made available under aCC-BY-NC 4.0 International license.

6. Foty, R. A. & Steinberg, M. S. The differential adhesion hypothesis: a direct evaluation. *Dev. Biol.* **278**, 255–263 (2005).
7. Harris, A. K. Is cell sorting caused by differences in the work of intercellular adhesion? A critique of the steinberg hypothesis. *J. Theor. Biol.* **61**, 267–285 (1976).
8. Brodland, G. W. The Differential Interfacial Tension Hypothesis (DITH): A Comprehensive Theory for the Self-Rearrangement of Embryonic Cells and Tissues. *J. Biomech. Eng.* **124**, 188–197 (2002).
9. Manning, M. L., Foty, R. A., Steinberg, M. S. & Schoetz, E.-M. Coaction of intercellular adhesion and cortical tension specifies tissue surface tension. *Proc. Natl. Acad. Sci.* **107**, 12517–12522 (2010).
10. Dahmann, C., Oates, A. C. & Brand, M. Boundary formation and maintenance in tissue development. *Nat. Rev. Genet.* **12**, 43–55 (2011).
11. Landsberg, K. P. *et al.* Increased Cell Bond Tension Governs Cell Sorting at the Drosophila Anteroposterior Compartment Boundary. *Curr. Biol.* **19**, 1950–1955 (2009).
12. Umetsu, D. *et al.* Local Increases in Mechanical Tension Shape Compartment Boundaries by Biasing Cell Intercalations. *Curr. Biol.* **24**, 1798–1805 (2014).
13. Balasubramaniam, L. *et al.* Investigating the nature of active forces in tissues reveals how contractile cells can form extensile monolayers. *Nat. Mater.* 1–11 (2021) doi:10.1038/s41563-021-00919-2.
14. Sahu, P. *et al.* Small-scale demixing in confluent biological tissues. *Soft Matter* **16**, 3325–3337 (2020).
15. Sussman, D. M., Schwarz, J. M., Marchetti, M. C. & Manning, M. L. Soft yet Sharp Interfaces in a Vertex Model of Confluent Tissue. *Phys. Rev. Lett.* **120**, 058001 (2018).
16. Krajnc, M. Solid–fluid transition and cell sorting in epithelia with junctional tension fluctuations. *Soft Matter* **16**, 3209–3215 (2020).
17. Gradeci, D. *et al.* Cell-scale biophysical determinants of cell competition in epithelia. *eLife* **10**, e61011 (2021).
18. Sato, K. & Umetsu, D. A Novel Cell Vertex Model Formulation that Distinguishes the Strength of Contraction Forces and Adhesion at Cell Boundaries. *Front. Phys.* **9**, 406 (2021).
19. Glazier, J. A. & Graner, F. Simulation of the differential adhesion driven rearrangement of biological cells. *Phys. Rev. E* **47**, 2128–2154 (1993).
20. Hirashima, T., Rens, E. G. & Merks, R. M. H. Cellular Potts modeling of complex multicellular behaviors in tissue morphogenesis. *Dev. Growth Differ.* **59**, 329–339 (2017).
21. Zhang, Y., Thomas, G. L., Swat, M., Shirinifard, A. & Glazier, J. A. Computer Simulations of Cell Sorting Due to Differential Adhesion. *PLOS ONE* **6**, e24999 (2011).
22. Fletcher, A. G., Osterfield, M., Baker, R. E. & Shvartsman, S. Y. Vertex Models of Epithelial Morphogenesis. *Biophys. J.* **106**, 2291–2304 (2014).

bioRxiv preprint doi: https://doi.org/10.1101/2022.05.23.492966; this version posted May 24, 2022. The copyright holder for this preprint (which was not certified by peer review) is the author/funder, who has granted bioRxiv a license to display the preprint in perpetuity. It is made available under aCC-BY-NC 4.0 International license.

23. Skamrahl, M. *et al.* Tight Junction ZO Proteins Maintain Tissue Fluidity, Ensuring Efficient Collective Cell Migration. *Adv. Sci.* **8**, 2100478 (2021).
24. Matsuzawa, K. *et al.* MAGIs regulate aPKC to enable balanced distribution of intercellular tension for epithelial sheet homeostasis. *Commun. Biol.* **4**, 1–11 (2021).
25. Janshoff, A. Viscoelastic properties of epithelial cells. *Biochem. Soc. Trans.* **49**, 2687–2695 (2021).
26. Cordes, A. *et al.* Prestress and Area Compressibility of Actin Cortices Determine the Viscoelastic Response of Living Cells. *Phys. Rev. Lett.* **125**, 068101 (2020).
27. Janshoff, A. Viscoelasticity of basal plasma membranes and cortices derived from MDCK II cells. *Biophys. Rep.* **1**, (2021).
28. Baum, B. & Georgiou, M. Dynamics of adherens junctions in epithelial establishment, maintenance, and remodeling. *J. Cell Biol.* **192**, 907–917 (2011).
29. Hatte, G., Prigent, C. & Tassan, J.-P. Tight junctions negatively regulate mechanical forces applied to adherens junctions in vertebrate epithelial tissue. *J. Cell Sci.* **131**, (2018).
30. Choi, W. *et al.* Remodeling the zonula adherens in response to tension and the role of afadin in this response. *J. Cell Biol.* **213**, 243–260 (2016).
31. Cartagena-Rivera, A. X., Van Itallie, C. M., Anderson, J. M. & Chadwick, R. S. Apical surface supracellular mechanical properties in polarized epithelium using noninvasive acoustic force spectroscopy. *Nat. Commun.* **8**, (2017).
32. Odenwald, M. A. *et al.* The scaffolding protein ZO-1 coordinates actomyosin and epithelial apical specializations *in vitro* and *in vivo*. *J. Biol. Chem.* **293**, 17317–17335 (2018).
33. Odenwald, M. A. *et al.* ZO-1 interactions with F-actin and occludin direct epithelial polarization and single lumen specification in 3D culture. *J. Cell Sci.* **130**, 243–259 (2017).
34. Fanning, A. S., Van Itallie, C. M. & Anderson, J. M. Zonula occludens-1 and -2 regulate apical cell structure and the zonula adherens cytoskeleton in polarized epithelia. *Mol. Biol. Cell* **23**, 577–590 (2011).
35. Bhide, S. *et al.* Mechanical competition alters the cellular interpretation of an endogenous genetic program. *J. Cell Biol.* **220**, e202104107 (2021).
36. Duguay, D., Foty, R. A. & Steinberg, M. S. Cadherin-mediated cell adhesion and tissue segregation: qualitative and quantitative determinants. *Dev. Biol.* **253**, 309–323 (2003).
37. Foty, R. A. & Steinberg, M. S. Cadherin-mediated cell-cell adhesion and tissue segregation in relation to malignancy. *Int. J. Dev. Biol.* **48**, 397–409 (2004).
38. Schötz, E.-M. *et al.* Quantitative differences in tissue surface tension influence zebrafish germ layer positioning. *HFSP J.* **2**, 42–56 (2008).

bioRxiv preprint doi: https://doi.org/10.1101/2022.05.23.492966; this version posted May 24, 2022. The copyright holder for this preprint (which was not certified by peer review) is the author/funder, who has granted bioRxiv a license to display the preprint in perpetuity. It is made available under aCC-BY-NC 4.0 International license.

39. Godt, D. & Tepass, U. Drosophila oocyte localization is mediated by differential cadherin-based adhesion. *Nature* **395**, 387–391 (1998).
40. Hayashi, T. & Carthew, R. W. Surface mechanics mediate pattern formation in the developing retina. *Nature* **431**, 647–652 (2004).
41. Ulrich, F. *et al.* Wnt11 Functions in Gastrulation by Controlling Cell Cohesion through Rab5c and E-Cadherin. *Dev. Cell* **9**, 555–564 (2005).
42. Kraft, B., Berger, C. D., Wallkamm, V., Steinbeisser, H. & Wedlich, D. Wnt-11 and Fz7 reduce cell adhesion in convergent extension by sequestration of PAPC and C-cadherin. *J. Cell Biol.* **198**, 695–709 (2012).
43. Vedula, S. R. K. *et al.* Quantifying Forces Mediated by Integral Tight Junction Proteins in Cell–Cell Adhesion. *Exp. Mech.* **49**, 3–9 (2009).
44. Krieg, M. *et al.* Tensile forces govern germ-layer organization in zebrafish. *Nat. Cell Biol.* **10**, 429–436 (2008).
45. Maitre, J.-L. *et al.* Adhesion Functions in Cell Sorting by Mechanically Coupling the Cortices of Adhering Cells. *Science* **338**, 253–256 (2012).
46. Wang, G., Manning, M. L. & Amack, J. D. Regional cell shape changes control form and function of Kupffer's vesicle in the zebrafish embryo. *Dev. Biol.* **370**, 52–62 (2012).
47. Amack, J. D. & Manning, M. L. Knowing the Boundaries: Extending the Differential Adhesion Hypothesis in Embryonic Cell Sorting. *Science* (2012) doi:10.1126/science.1223953.
48. Liu, Z. *et al.* Mechanical tugging force regulates the size of cell-cell junctions. *Proc. Natl. Acad. Sci.* **107**, 9944–9949 (2010).
49. Koirala, R. *et al.* Inside-out regulation of E-cadherin conformation and adhesion. *Proc. Natl. Acad. Sci.* **118**, (2021).
50. Seddiki, R. *et al.* Force-dependent binding of vinculin to α-catenin regulates cell–cell contact stability and collective cell behavior. *Mol. Biol. Cell* **29**, 380–388 (2018).
51. Reffay, M. *et al.* Interplay of RhoA and mechanical forces in collective cell migration driven by leader cells. *Nat. Cell Biol.* **16**, 217–223 (2014).
52. FAK suppresses Rho activity to promote focal adhesion turnover. 7.
53. Yin, J. & Yu, F.-S. X. Rho kinases regulate corneal epithelial wound healing. *Am. J. Physiol.-Cell Physiol.* **295**, C378–C387 (2008).
54. Wyatt, T., Baum, B. & Charras, G. A question of time: tissue adaptation to mechanical forces. *Curr. Opin. Cell Biol.* **38**, 68–73 (2016).

bioRxiv preprint doi: https://doi.org/10.1101/2022.05.23.492966; this version posted May 24, 2022. The copyright holder for this preprint (which was not certified by peer review) is the author/funder, who has granted bioRxiv a license to display the preprint in perpetuity. It is made available under aCC-BY-NC 4.0 International license.

55. Beutel, O., Maraspini, R., Pombo-García, K., Martin-Lemaitre, C. & Honigmann, A. Phase Separation of Zonula Occludens Proteins Drives Formation of Tight Junctions. *Cell* **179**, 923-936.e11 (2019).

56. Schindelin, J. *et al.* Fiji: an open-source platform for biological-image analysis. *Nat. Methods* **9**, 676–682 (2012).

57. Stringer, C., Wang, T., Michaelos, M. & Pachitariu, M. Cellpose: a generalist algorithm for cellular segmentation. *Nat. Methods* 1–7 (2020) doi:10.1038/s41592-020-01018-x.

58. BRADSKI, G. The OpenCV library. *Dr Dobbs J Softw. Tools* **25**, 120–125 (2000).

59. Teh, C.- & Chin, R. T. On the detection of dominant points on digital curves. *IEEE Trans. Pattern Anal. Mach. Intell.* **11**, 859–872 (1989).

60. Crocker, J. C. & Grier, D. G. Methods of Digital Video Microscopy for Colloidal Studies. *J. Colloid Interface Sci.* **179**, 298–310 (1996).

61. Hutter, J. L. & Bechhoefer, J. Calibration of atomic-force microscope tips. *Rev. Sci. Instrum.* **64**, 1868–1873 (1993).

bioRxiv preprint doi: https://doi.org/10.1101/2022.05.23.492966; this version posted May 24, 2022. The copyright holder for this preprint (which was not certified by peer review) is the author/funder, who has granted bioRxiv a license to display the preprint in perpetuity. It is made available under aCC-BY-NC 4.0 International license.

Supporting information

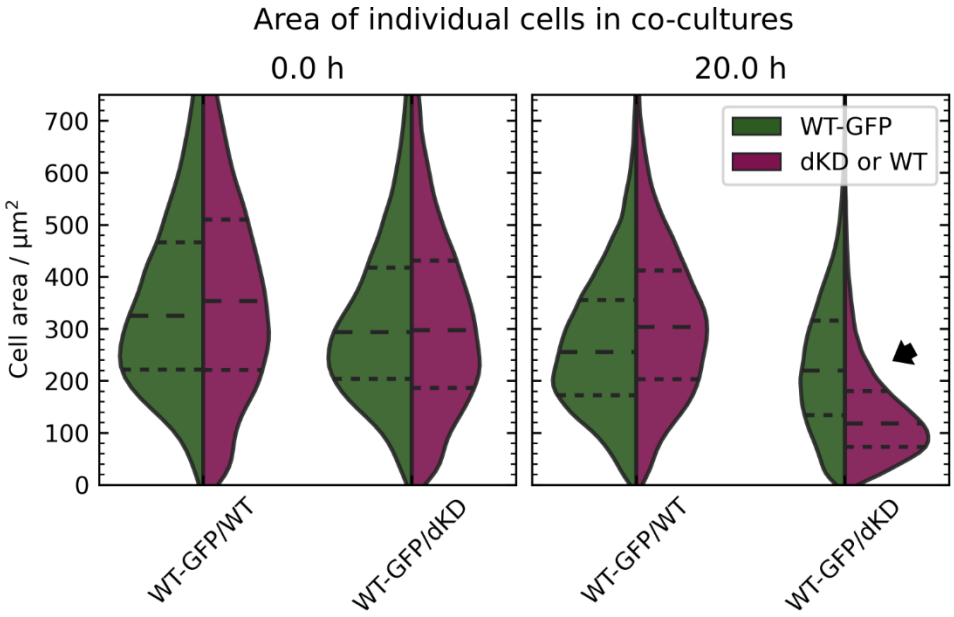

Figure S1. Area of individual cells in the co-cultures from Figure 1. Violin plots are shown, depicting the kernel density estimation with horizontal, dashed lines showing the quartiles and median. Violins are scaled to have the same area. The arrow indicates the unique area offset in WT/dKD co-cultures due to differential contractility.

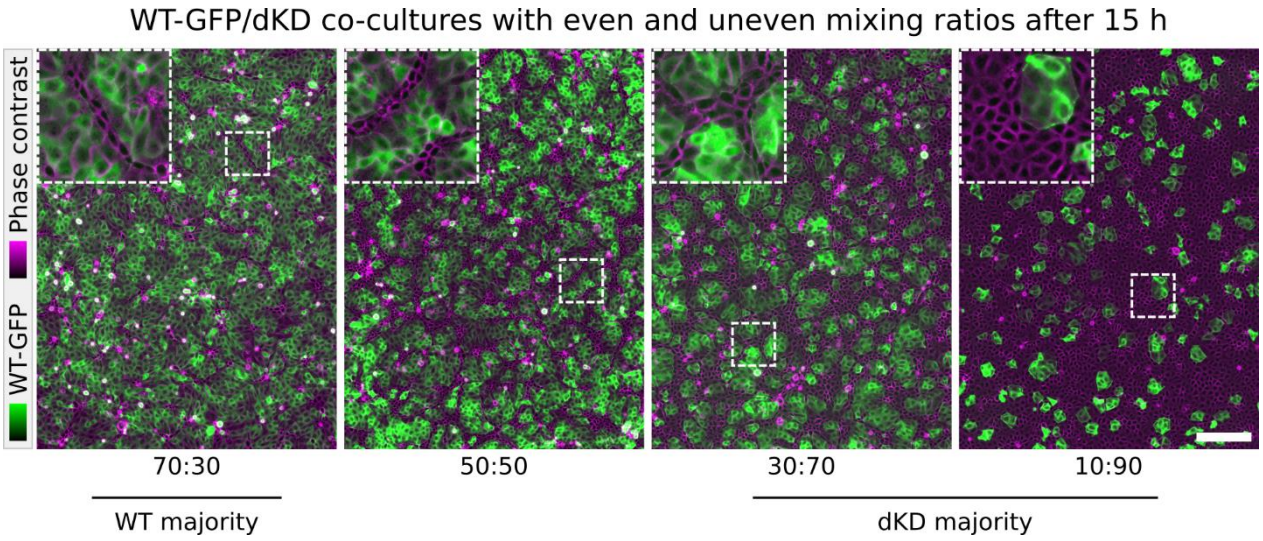

Figure S2. Demixing WT/dKD co-culture experiments performed as in Figure 1 after 15 h of incubation, seeded at even and uneven mixing ratios. Scale bar 200 µm.

bioRxiv preprint doi: https://doi.org/10.1101/2022.05.23.492966; this version posted May 24, 2022. The copyright holder for this preprint (which was not certified by peer review) is the author/funder, who has granted bioRxiv a license to display the preprint in perpetuity. It is made available under aCC-BY-NC 4.0 International license.

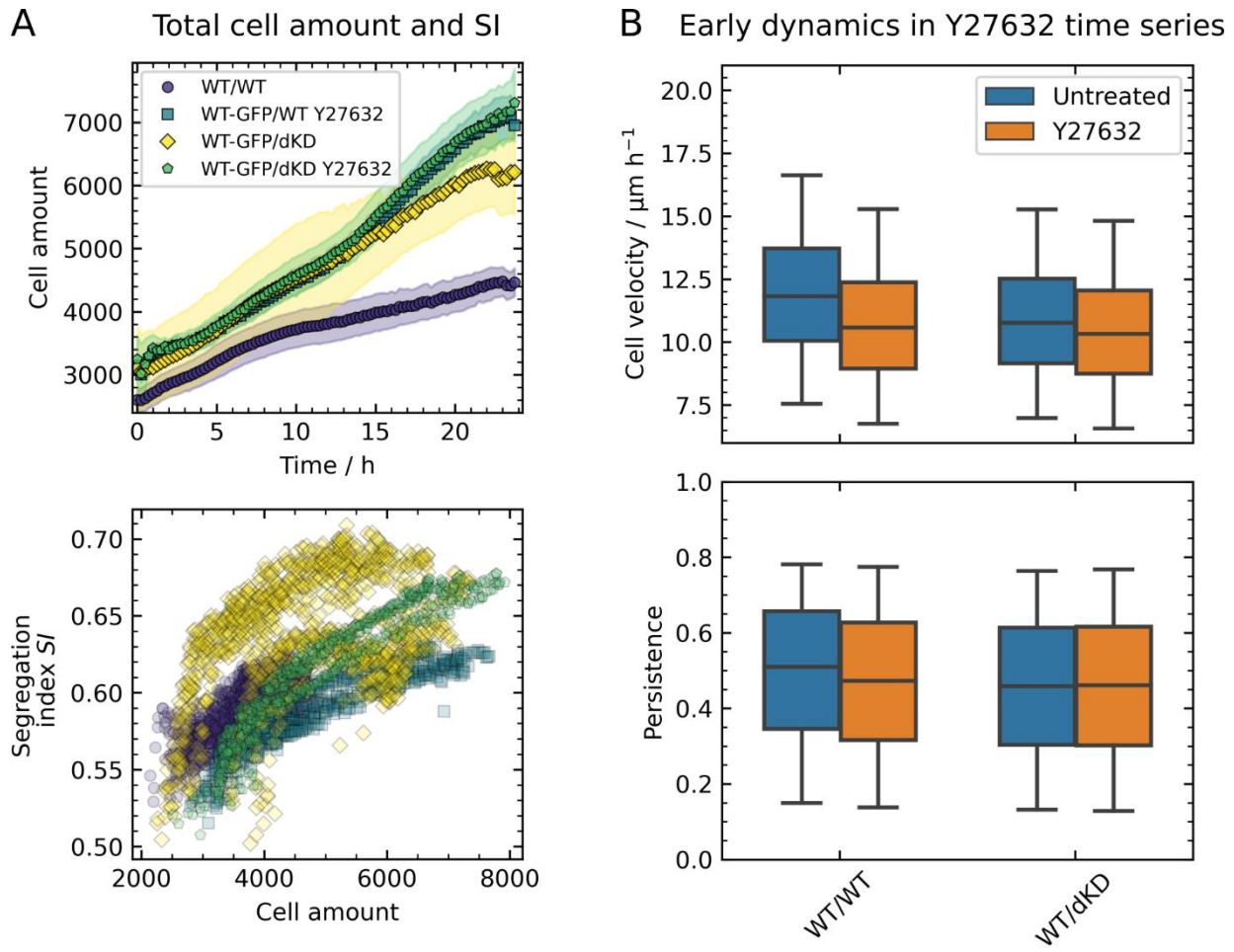

Figure S3. Additional analyses of the co-culture (de-) mixing experiments from Figure 1 and 5. A) Total cell amount over time and the *SI* plotted against the total cell amount. B) Velocity and persistence within the first 5 h after seeding. Both parameters were calculated from individual cell tracks. Velocity was averaged over all frames. Persistence was defined as the ratio of the direct distance between the start- and endpoint and the sum of the distances traveled in each step.